An HST Study of the Substellar Population of NGC 2024

Citation for the original published paper (version of record):
Robberto, M., Gennaro, M., Da Rio, N. et al (2024). An HST Study of the Substellar Population of NGC 2024. Astrophysical Journal, 960(1). http://dx.doi.org/10.3847/1538-4357/ad0785

The Astrophysical Journal, 960:49 (19pp), 2024 January 1 https://doi.org/10.3847/1538-4357/ad0785

An HST Study of the Substellar Population of NGC 2024

Massimo Robberto[1,2,6], Mario Gennaro[1,2], Nicola Da Rio[3], Giovanni Maria Strampelli[1,2,4], Leonardo Ubeda[1],
Elena Sabbi[1], Dana Koeppe[2], Jonathan C. Tan[3,5], and David R. Soderblom[1]
[1] Space Telescope Science Institute, 3700 San Martin Drive, Baltimore, MD 21218, USA; robberto@stsci.edu
[2] Johns Hopkins University, 3400 N. Charles Street, Baltimore, MD 21218, USA
[3] Dept. of Astronomy, University of Virginia, Charlottesville, Virginia, USA
[4] Department of Astrophysics, University of La Laguna, Av. Astrofísico Francisco Sánchez, E-38200 San Cristóbal de La Laguna, Tenerife, Canary Islands, Spain
[5] Department of Space, Earth and Environment, Chalmers University of Technology, Gothenburg, Sweden

Received 2023 April 16; revised 2023 October 1; accepted 2023 October 1; published 2023 December 21

Abstract

We performed an HST/WFC3-IR imaging survey of the young stellar cluster NGC 2024 in three filters probing the 1.4 μm H_2O absorption feature, characteristic of the population of low-mass and substellar-mass objects down to a few Jupiter masses. We detect 812 point sources, 550 of them in all three filters with signal-to-noise ratio greater than 5. Using a distance-independent two-color diagram, we determine extinction values as high as $A_V \simeq 40$. We also find that the change of effective wavelengths in our filters results in higher A_V values as the reddening increases. Reconstructing a dereddened color–magnitude diagram, we derive a luminosity histogram both for the full sample of candidate cluster members and for an extinction-limited subsample containing the 50% of sources with $A_V \lesssim 15$. Assuming a standard extinction law like Cardelli et al. with a nominal $R_V = 3.1$, we produce a luminosity function in good agreement with the one resulting from a Salpeter-like initial mass function for a 1 Myr isochrone. There is some evidence of an excess of luminous stars in the most embedded region. We posit that the correlation may be due to those sources being younger, and therefore overluminous, than the more evolved and less extincted cluster's stars. We compare our classification scheme based on the depth of the 1.4 μm photometric feature with the results from the spectroscopic survey of Levine et al., and we report a few peculiar sources and morphological features typical of the rich phenomenology commonly encountered in young star-forming regions.

Unified Astronomy Thesaurus concepts: Young massive clusters (2049); Pre-main sequence stars (1290); Star formation (1569)

Supporting material: machine-readable tables

1. Introduction

Observations of the youngest stellar clusters in the solar vicinity provide unique insights into the phenomenon of star formation (Lada & Lada 2003). Stellar systems with ages less than their dynamical timescales preserve the original characteristics imprinted by the star formation process, allowing direct comparison of the basic physical and dynamical parameters of their members with those of prestellar cores in giant molecular clouds, and with theoretical models (Krumholz et al. 2019). On the other hand, rich young clusters may be strongly affected by feedback from their massive stars. Through photoevaporation and stellar winds, the large amounts of radiative and mechanical energy released by massive stars play an accumulative role in the process of star and planet formation (Störzer & Hollenbach 1999; Dib et al. 2010; Winter et al. 2020) as well as in the cluster dynamics through the dispersal of diffuse material and the resulting decrease in gravitational binding energy (Grudić et al. 2018) with the loss of more than 50% of stars (Brinkmann et al. 2017). At the same time, the high stellar density at the cluster center may cause close encounters with explosive ejections of runaway stars (Rivera-Ortiz et al. 2021) as well as protoplanetary disk fragmentation, again combined with ejection (Whitworth & Bate 2007; Bonnell et al. 2008; Stamatellos & Whitworth 2009). The majority of low-mass stars are especially sensitive to these effects, and measuring their global properties, with their variations both within and between different clusters, may clarify the frequency and relevance of these complex physical processes.

A key parameter is the low-mass initial mass function (IMF), often parameterized using the canonical Chabrier or Kroupa forms established for the Milky Way disk. In the substellar regime, however, the IMF is difficult to characterize due to a multitude of factors (Offner et al. 2013; Hopkins 2018). This is reflected in the original broken power law of Kroupa (2001), which has an α exponent with large uncertainty, i.e., $\alpha = 0.3 \pm 0.7$ in the mass range $0.01 \leqslant m/M_\odot \leqslant 0.08$. While studies of different clusters in the solar vicinity, e.g., the Orion Nebula Cluster (ONC; Gennaro & Robberto 2020), NGC 2244, (Almendros-Abad et al. 2023), Chamaeleon I (Luhman 2007), λ Ori (Bayo et al. 2011), σ Ori (Peña et al. 2012; Damian et al. 2023), ρ Ophiuchi (Oliveira et al. 2012), Upper Scorpius (Lodieu 2013), NGC 1333 and IC 348 (Scholz et al. 2013), Lupus 3 (Mužić et al. 2015), and 25 Ori (Downes et al. 2014; Suárez et al. 2019), report IMFs generally consistent with the canonical laws, a number of studies (Weidner et al. 2013; Dib 2014; Dib et al. 2017) provide statistically significant evidence of variations of IMF between clusters. A spread of

---

[6] Based on observations made with the NASA/ESA Hubble Space Telescope, obtained at the Space Telescope Science Institute, which is operated by the Association of Universities for Research in Astronomy, Inc., under NASA contract NAS 5-26555. These observations are associated with program HST-GO-15334.002-A.

IMF parameters may actually explain the integrated IMF of galaxies of different metallicity (Dib 2022).

Among the closest young clusters, the one associated with the "Flame Nebula," NGC 2024, plays a special role, often being regarded as a young, downsized version of the more extensively studied ONC. Both are located at nearly the same ∼400 pc distance and in the same complex of molecular clouds, NGC 2024 representing the richest star-forming region in the Orion-B molecular cloud (Meyer et al. 2008), while the ONC is the richest young cluster in the Orion-A molecular cloud. The age of NGC 2024, ∼0.5 Myr as determined by early near-infrared photometric studies (e.g., Comeron et al. 1996; Meyer 1996; Haisch & Lada 2000) is less than that of the ONC (∼1–3 Myr), consistent with the fact that NGC 2024 appears more heavily obscured. Its morphology at visible wavelengths is dominated by a north–south dark lane of high opacity ($A_V \simeq 20$ mag; Skinner et al. 2003), the densest part of a foreground dust layer causing extreme differential extinction across the field (Barnes et al. 1989). Performing photometry at near-IR wavelengths, Meyer (1996) found that the majority of cluster members, ≃70%, harbor accreting disks. Using the NICMOS-3 camera on board the Hubble Space Telescope (HST), Liu et al. (2003) imaged the inner 4.27 square arcminutes of NGC 2024 in the F110W and F160W filters. Their photometry of 79 sources indicates a ratio of intermediate- to low-mass objects consistent with the field IMF. Following the photometric observations, Levine et al. (2006) spectroscopically probed the low-mass/substellar candidates, finding that out of 70 spectra, ∼15 can be interpreted as substellar objects. Penetrating the dust lane at longer wavelengths, Spitzer/IRAC images unveiled that the young stellar cluster reaches a stellar density $n_* \simeq 2000$ pc^{-3} (Megeath et al. 2005). Rich, young clusters are typically dominated by a few massive stars. In the case of NGC 2024, the main ionizing source is currently considered to be IRS 2b, a highly reddened late-O type star (Bik et al. 2003 reported an ∼O8 spectral type) to the east of the dark lane and slightly off-center with respect to the bulk of the general young stellar population. More recently, van Terwisga et al. (2020) used the Atacama Large Millimeter/submillimeter Array to survey at 1.3 mm in the central 2.′9 × 2.′9 region, detecting 179 disks. They find that disks at the smallest projected distance from IRS 2b appear younger and more massive than those to the west of the dark lane, a region of lower extinctions dominated by a less massive B0.V star, IRS 1. Using archival HST images, Haworth et al. (2021) showed that photoevaporated disks (proplyds) can be found in both regions, with ionized cusps pointing to both IRS 1 and IRS 2b, indicating that both sources are primary actors in the external photoevaporation of disks in NGC 2024.

In order to improve the census of the NGC 2024 cluster in the substellar mass regime, we have performed a near-IR imaging survey adopting a multiband photometry technique that allows us to estimate the temperature of sources with $T_{\rm eff} \lesssim 3200$ K. Compared to the more accurate infrared spectroscopy, multiband photometry has two main advantages: (1) observing efficiency, as hundreds of sources can be simultaneously observed with high signal-to-noise ratio (S/N), and (2) lack of bias, as the entire cluster can be sampled down to a certain (mass-dependent) extinction level, without preselection of the targets.

The primary spectral features probing the temperature range typical of low-mass stars and brown dwarfs are arguably the H_2O and CH_4 near-infrared bands. These bands are hardly measurable from the ground because of the strength and variability of telluric absorption, but are fully accessible with space-based instruments like the WFC3/IR on the HST. In a previous study of the ONC, Robberto et al. (2020) used the WFC3/IR F130N and F139M photometric bands to build a spectral index tracing the depth of the H_2O absorption feature at $\lambda \simeq 1.4\ \mu$m. In the case of the ONC, this technique allows the population of low-mass stars to be efficiently disentangled from the contamination of Galactic and extragalactic objects, which is significant at the faint magnitude levels of the young planetary-mass objects.

Here, we present the results obtained by performing a similar survey in the NGC 2024 region. For this study, a third filter close in wavelength to our other two filters, the "wide Y" F105W bandpass, has been added to produce a distance-independent two-color diagram useful for assessing the substantial reddening toward each source while minimizing the risk of contamination from thermal IR excess due to circumstellar disks.

This paper is organized as follows: in Section 2 we present our observing strategy and data reduction methodology. In Section 3 we present our results, i.e., the main photometric catalog and the color–magnitude diagram (CMD), the extinction estimated from the color–color diagram, and the luminosity function from the dereddened version of a CMD. In Section 4 we compare the quantities extracted from our 1.4 μm index with those derived using spectroscopy by Levine et al. (2006). Finally, in Section 5 we summarize our findings, and in the Appendix we introduce a few noticeable objects and morphological features revealed by our visual inspection of the images.

2. Observations and Data Processing

The observations presented here are part of the HST GO-15334 program (Principal Investigator N. Da Rio). They have been executed with the Wide Field Camera 3 on board the HST between 2018 October and 2020 April. Twenty orbits were allocated to produce a mosaic of 5 × 4 WFC3/IR pointings, as shown in Figure 1. To maximize areal coverage and maintain uniformity of exposure time across the field, the overlap between individual tiles was kept to a minimum. However, the original plan of building a mosaic without gaps was hampered by the difficulty of finding suitable guide stars at the optimal telescope pointings and orientations. Iterating with the HST program coordinators at the Space Telescope Science Institute, we were finally able to craft a configuration that leaves only a small fraction of the field uncovered. Overall, the survey extends over 84.57 square arcminutes centered on R.A. = 05:41:42.945 and decl. = −1:54:18.58 (J2000). For comparison, this is about 17% of the area covered by the HST GO-13826 program on the ONC.

The filters used were F130N, F139M, and F105W. The exposure times were different for each filter and were determined considering the different widths of the three passbands in order to achieve S/N in all filters. For the narrowband F130N filter, the longer exposure time was split into two halves to limit the influence of cosmic rays. At each pointing, three slightly dithered exposures were taken for each

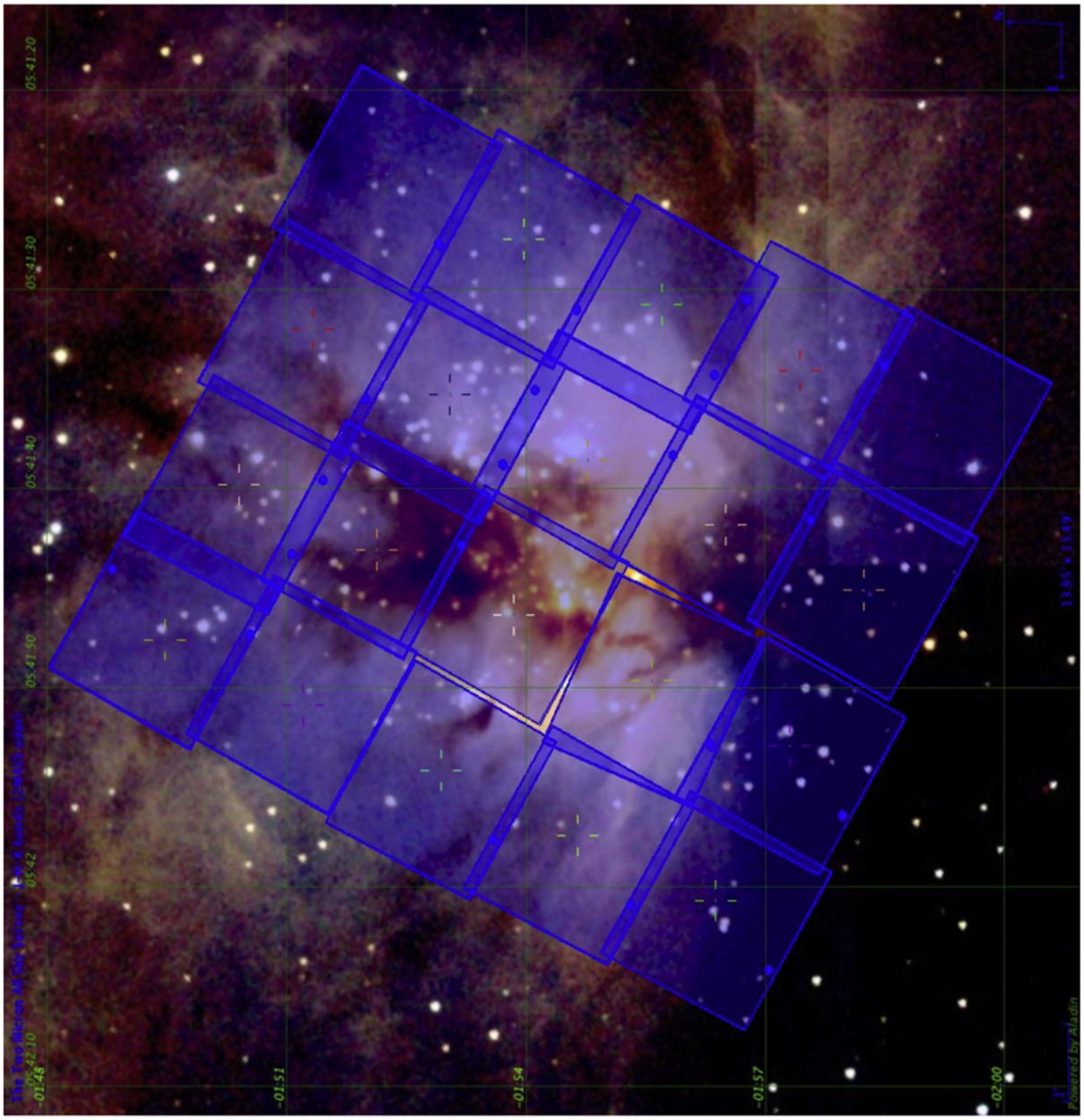

Figure 1. Footprint of the NGC 2024 data set presented in this paper, overlaid on the 2MASS image of the field.

filter to mitigate against bad pixels and cosmic rays. The readout parameters are presented in Table 1.

The images were registered against the GAIA-DR1 (Gaia Collaboration et al. 2016a, 2016b)[7] catalog and drizzled to the nominal WFC3/IR pixel scale of 0.″12825 pixel^{-1}. Figure 2 shows the final mosaic obtained by combining the three filters as an RGB color composite image.

An initial source catalog was obtained using the Dolphot package (Dolphin 2000, 2016) on the 20 dithered exposures of each visit. Visual inspection of the final drizzled images was necessary to eliminate residual artifacts due to persistence and confirm a few objects with low S/N. We present the results obtained by performing aperture photometry on the final drizzled images, with an extraction aperture of 0.″4 and the most recent (year 2020) release of the WFC3-IR zero-points (Bajaj et al. 2020). Since the new zero-points are provided for infinite aperture, we adopted the aperture corrections given by the previous 2012 calibration. As a result, the magnitudes determined using a 0.″4 aperture radius on the drizzled images were corrected to Vega magnitudes using the following zero-points: ZP(130N) = 21.797, ZP(F139M) = 23.175, and ZP(F105W) = 25.432.

Table 1
WFC3 Detector Readout Parameters

Filter	Readout Pattern	$N_{\rm samp}$	Exp. Time/ Pointing (s)	Exp. Time/ Visit (s)
F130N	SPARS-50	7	2 × 303	1817
F139M	SPARS-25	6	128	385.8
F105W	SPARS-10	5	43	128.8

Figure 3 shows the distribution of photometric uncertainty, *dm*, versus magnitude, *m*, in the Vega system for the sources

---

[7] GAIA-DR1 was the version available when data were processed. Since the differences between DR1 and DR2 are negligible for our goals, we have maintained our original astrometric solution throughout the analysis.

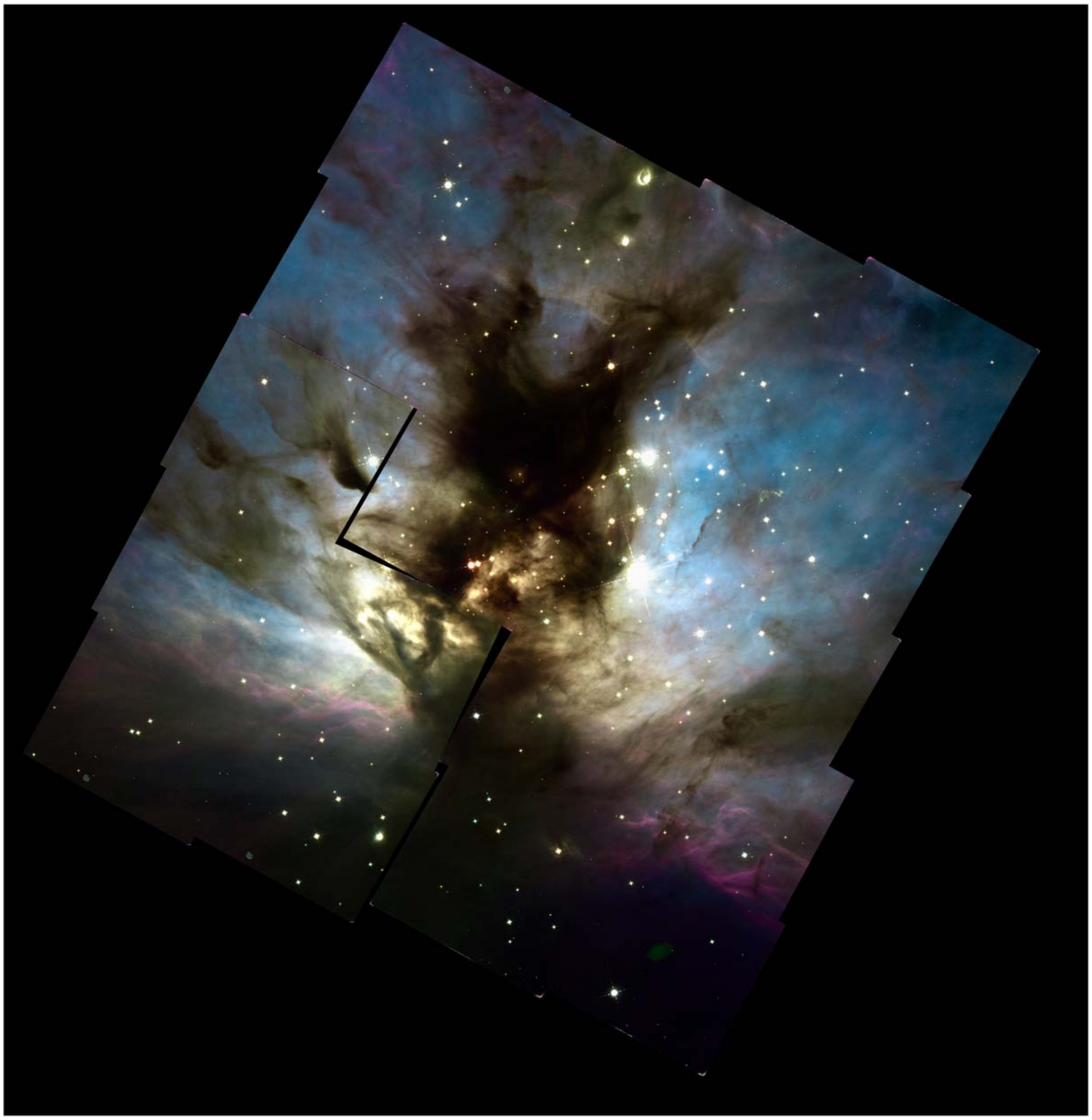

Figure 2. Color composite mosaic obtained by combining in the RGB planes the F139M, F130N, and F105W drizzled images, in the order of R=F139M, G=F130N and B=F105W.

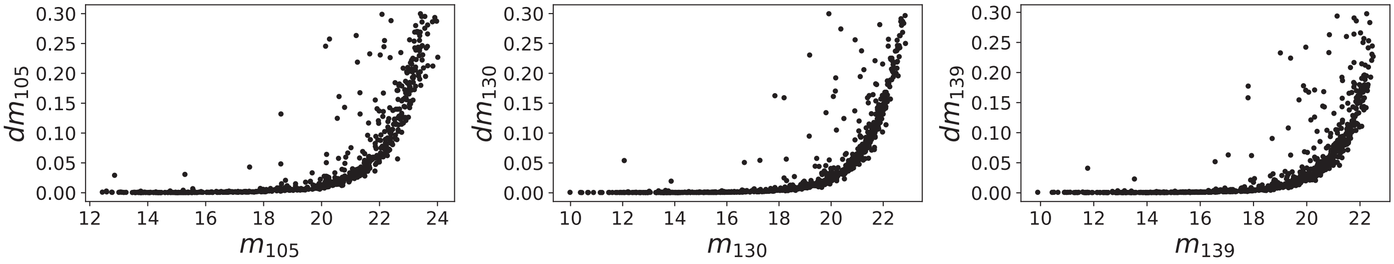

Figure 3. Distribution of the photometric uncertainty vs. magnitude for the three filters in the Vega system.

detected with $dm < 0.3$ mag ($S/N \gtrsim 3$). There are 618 sources in the F105W filter, 761 in the F130N, and 800 in the F139M.

Our sensitivity limits are not uniform across the field. To assess their spatial variation we randomly injected 90,000 sources with magnitudes in the range 21–25, retrieved their flux using aperture photometry as for the real sources, and estimated the number of sources measured with $S/N > 3$ at different magnitude thresholds. Figure 4 shows how the fraction of recovered sources drops when moving to fainter magnitudes, reaching 50% at approximately $m_{105\mathrm{W}} = 23.5$, $m_{130\mathrm{N}} = 22.4$, and $m_{139\mathrm{M}} = 21.6$ on average across the field, but with significant spatial variations.

The map in Figure 5, relative to the F105W filter, shows how the sensitivity at the 3σ level decreases by a couple of

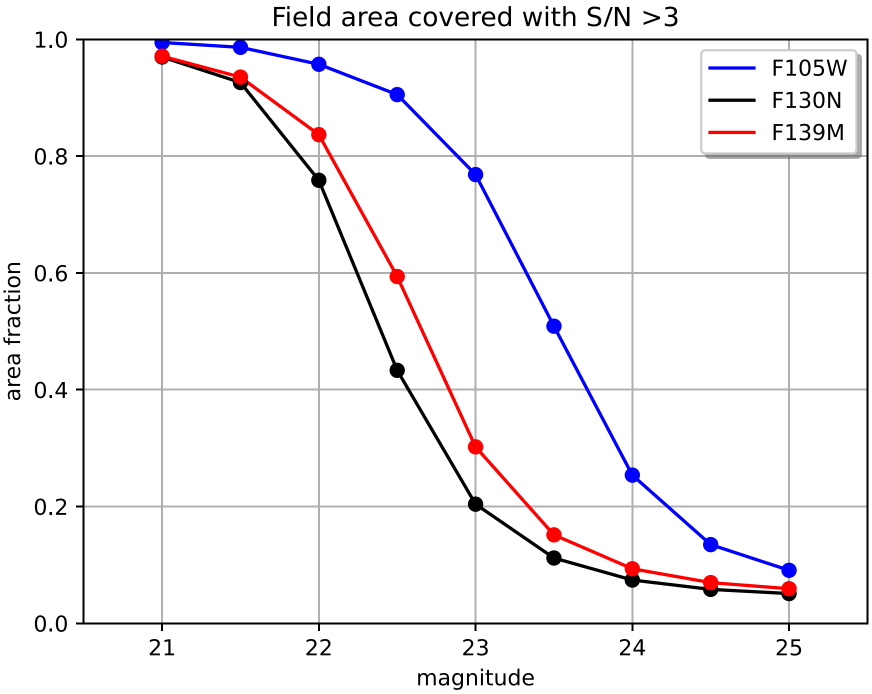

Figure 4. Fraction of the survey area covered with $S/N > 3$ vs. magnitude in the three passbands.

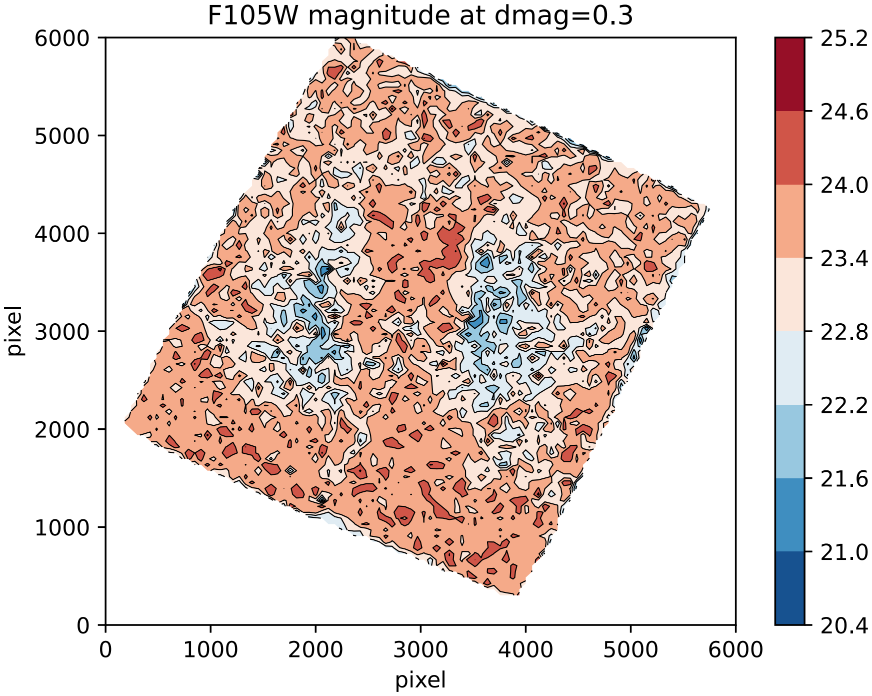

Figure 5. Spatial distribution of the limit magnitude in the F105W filter.

magnitudes in correspondence with the brightest regions due to the increased background. Similar maps are obtained for the other two filters. In practice, the darkest regions—those with the lowest source density due to high extinction—are also those where our detection threshold increases, and vice versa for the brightest regions. Therefore, the completeness of our source catalog, intended as the number of sources detected versus the number of cluster members, is predominantly determined by extinction to the cluster and cannot be recovered using a sensitivity map, unlike when completeness is determined, e.g., by source confusion.

At the bright end, all sources are accounted for in our catalog with the exception of source IRS 5 of Barnes et al. (1989), as it falls right in a gap between our tiles. This is one of the brightest

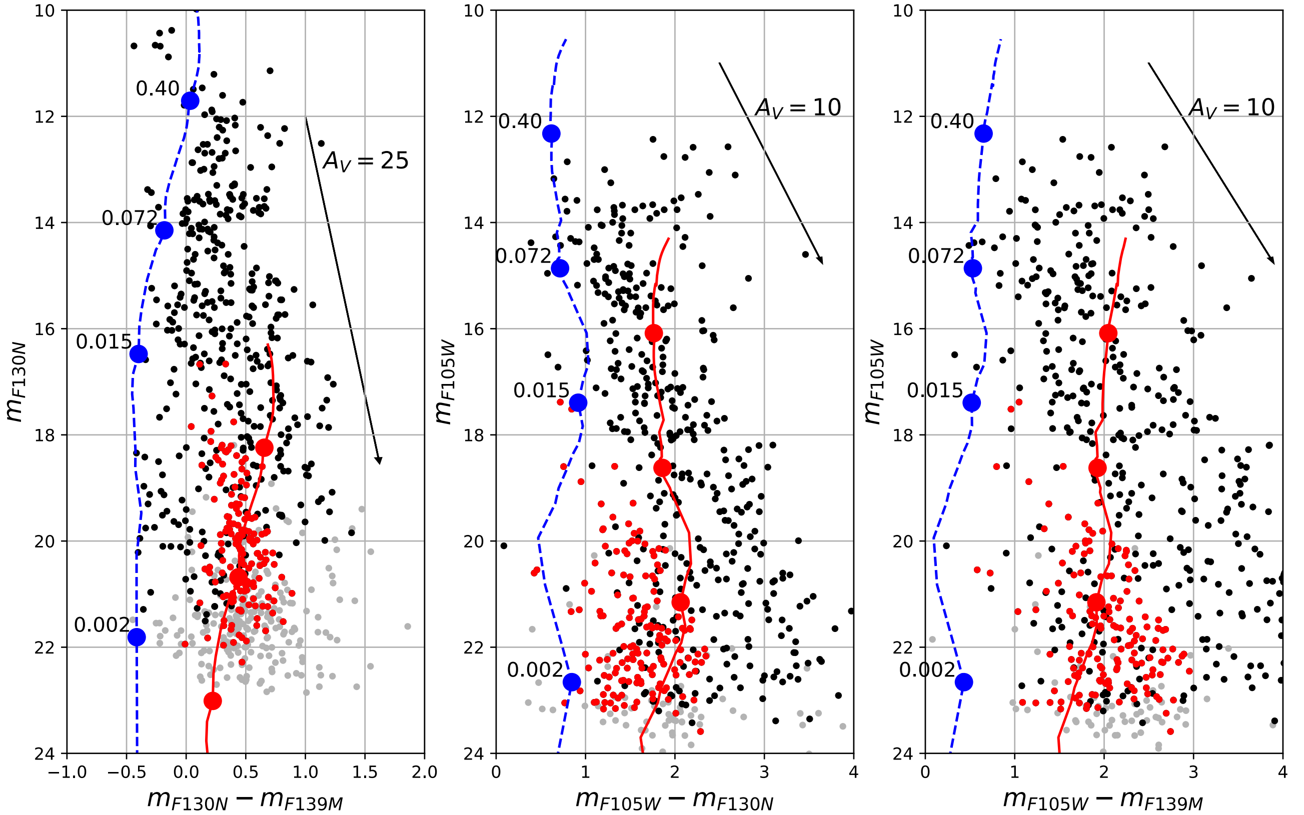

Figure 6. CMDs for all sources in our catalog with uncertainty $dm \leqslant 0.2$ mag in all filters (black dots). Sources with larger uncertainty up to $dm = 0.3$ mag, generally at the bottom of each diagram, are shown as gray dots. The red dots indicate candidate background sources selected according to the diagram shown in Figure 7. The blue dashed lines are the 1 Myr isochrones according to the BT-Settl models, modified in the F139M passband as in Robberto et al. (2020). The red solid line shows the same isochrone with $A_V = 10$ magnitudes of reddening according to the standard Cardelli et al. (1989) law with $R_V = 3.1$, the corresponding vector being represented by an arrow. The filled circles on the isochrones, top to bottom, indicate the locus of objects of mass 0.4, 0.72, 0.015, and 0.002 $M_\odot$.

Table 2
WFC3-IR Photometry from the HST GO-15334 Program

Entry Number	R.A. (J2000)	Decl. (J2000)	m_105	dm_105	m_130	dm_130	m_139	dm_139
1	85.396685	−2.008753	22.640	0.156	21.507	0.102	21.347	0.094
2	85.396449	−2.008472	23.373	0.230	21.383	0.076	21.285	0.073
3	85.398049	−2.007868	19.287	0.007	17.755	0.004	17.357	0.002
…	…	…	…	…	…	…	…	…

(This table is available in its entirety in machine-readable form.)

near-infrared sources in the field with Two Micron All Sky Survey (2MASS) magnitudes $J = 10.35$, $H = 8.53$, and $K = 7.54$ (Cutri et al. 2003).

The full photometric catalog, containing 812 entries, is presented in Table 2. From left to right, the columns show our entry number, the R.A. and decl. at the J2000.0 epoch, and the Vega-system magnitudes and associated uncertainties in the F105W, F130N, and F139M filters. In the following sections we shall concentrate on the 550 sources with magnitude uncertainties <0.2 mag in all three filters.

3. Results

3.1. Color–Magnitude Diagrams

By combining the three filter pairs, one can produce the CMDs presented in Figure 6. On each CMD we overplot the unreddened 1 Myr isochrones at 400 pc from the BT-Settl family of models (blue dashed lines) with four representative points corresponding to 0.4, 0.072, 0.015, and 0.002 $M_\odot$ stars, top to bottom. Assuming no extinction, the highest value roughly corresponds to our saturation limits, the lowest value corresponds to our detection limits, and the intermediate values are representative of the hydrogen and deuterium burning limits.

The first of the three diagrams, the F130N – F139M CMD, presents on the horizontal axis our H_2O index and was derived also for the ONC by Robberto et al. (2020). They found that the BT-Settl isochrone calculated down to 0.5 $M_{\rm Jup}$ predicts highly negative (blue) H_2O color as one approaches the lowest masses. Our new diagram for NGC 2024 is consistent with those findings, in the sense that there are no sources with color F130N − F139M bluer than −0.5. To match the ONC observations, Robberto et al. (2020) applied a correction to the magnitude of the BT-Settl isochrone in the F130N filters, and we shall adopt the same recipe here. The discrepancy between theory and observations might be attributed to the incomplete line lists and opacity tables used to predict the water absorption feature for objects with very low effective temperature and surface gravity. Historically, the shape of the spectra of very young and very low-mass objects in the 1.4 μm region has always been difficult to probe from the ground due to telluric absorption of water vapor. The paucity of observational benchmarks reflects the accuracy of theoretical models at these wavelengths, a situation that is certainly going to change once new JWST observations become available.

The slope of the reddening vectors, also shown in the figure, has been determined using Synphot (STScI Development Team 2018) to calculate the change in the Vega spectrum in our passbands when adopting the Milky Way $R_V = 3.1$ reddening law of Cardelli et al. (1989). We estimate that an extinction $A_V = 5$ mag in the standard Johnson V bandpass corresponds to $A_{105W} = 1.88$, $A_{130N} = 1.31$, and $A_{139M} = 1.18$ mag, and the lines have been drawn according to these values.

Guided by the reddening vectors, one can discern that the main distribution of sources appears compatible with a heavily reddened IMF, peaking in the mass bin 0.075–0.40 $M_\odot$ and spreading to higher magnitudes and redder colors, i.e., to the bottom right. If one compares the three diagrams, however, an anomaly becomes apparent: the clumps of points in the lower half of the diagrams cannot be reconciled with the isochrone when assuming a similar amount of extinction. In fact, in order to match the highest density of sources, the three reddened isochrones, represented in the plots as red solid lines, had to be traced assuming $A_V = 25$ in the first plot and $A_V = 10$ in both the second and third plots. The strong discrepancy in A_V values means those sources cannot be simply interpreted as reddened young stars, but represent instead the population of background Galactic sources "leaking" through the nebular background. Comparing the first CMD with the similar one presented by Robberto et al. (2020), one can see that the locus of this population is consistent with that already found for the ONC.

To discriminate more rigorously the cluster sources from the contaminants, we have looked at the discrepancy between the extinction values. Dereddening each source to the 1 Myr isochrone, one determines three different A_V values, one for each plot. Plotting the largest difference (max. − min.) versus minimum difference (central − min.) of each A_V trio, one can draw a region encompassing sources that present a large outlier, i.e., with the first difference much larger than the second one; see Figure 7. This results in 179 sources concentrated in the lower parts of the CMDs (red dots in Figure 6), which we shall regard as candidate Galactic contaminants. Consequently, we are left with 371 candidate cluster sources.

Returning our attention the first CMD of Figure 6, one can see that none of these candidate background sources has negative H_2O index. All the faint objects with negative H_2O color index lying parallel to the blue isochrones remain identified as candidate cluster stars. They most probably represent the fraction of very low-mass sources, down to planetary masses, detected by our survey. Their location in the diagram is consistent with that of the objects detected in the ONC, albeit in lower number due to the large and nonuniform extinction across the field and the more modest statistics for this less rich cluster, and considering also our smaller survey area.

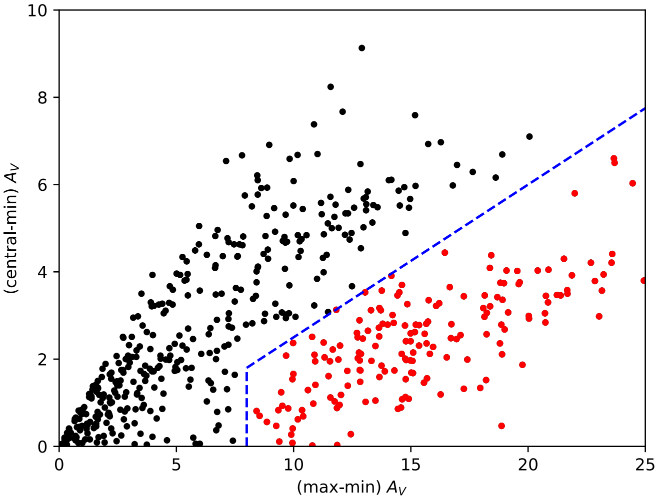

Figure 7. Largest vs. smallest difference between the three A_V values determined by dereddening each source to the 1 Myr isochrones in Figure 6. Red dots indicate the sources showing the largest discrepancy (i.e., a large outlier), which can be considered as candidate background sources.

3.2. Color–Color Diagram and Extinction

The availability of a third photometric band allows one to create a distance-independent (F130N − F139M) versus (F105W − F130N) color–color diagram, shown in Figure 8, for the subset of 550 targets having uncertainties smaller than 0.2 mag in all three filters. The 1 Myr isochrone, drawn as a blue solid line for masses ranging from 1.4 $M_\odot$ to 0.002 $M_\odot$, spans a rather narrow range of colors, as expected due to the nearly adjacent wavelengths; note the negative values of the (F130N − F139M) index for $M < 0.4\,M_\odot$ due to the H_2O absorption feature.

Overall, the source distribution is dominated by extinction, the points spreading up and to the right toward reddened colors. The two straight lines trace the reddening corresponding to the Cardelli et al. (1989) $R = 3.1$ extinction law, estimated at the nominal filter wavelengths of 1.05 μm, 1.30 μm, and 1.39 μm, as explained in the previous section. Assuming our passbands are not significantly contaminated by non-photospheric emission, these lines should enclose the area occupied by reddened low-mass cluster members. Note, however, that our candidate cluster sources (black dots) and background sources (red dots) largely overlap in the diagram, which therefore cannot be used to further discriminate the two populations.

It is also clear that the straight lines fail to explain the main distribution of sources, as they are spread in a direction less steep than that predicted by our reddening vector. We have verified that other reddening laws trace straight lines that are not significantly different from the Cardelli et al. (1989) vector, as expected due to the limited spectral coverage of our passbands and the relative uniformity of reddening laws in the near IR.

The mismatch between the standard reddening vectors and the source distribution in our diagram can be reconciled if one observes that in the case of NGC 2024 we are dealing with extremely high values of extinction. For any given reddening law, as extinction increases and the spectral energy distribution becomes redder and redder, one has to account for the change

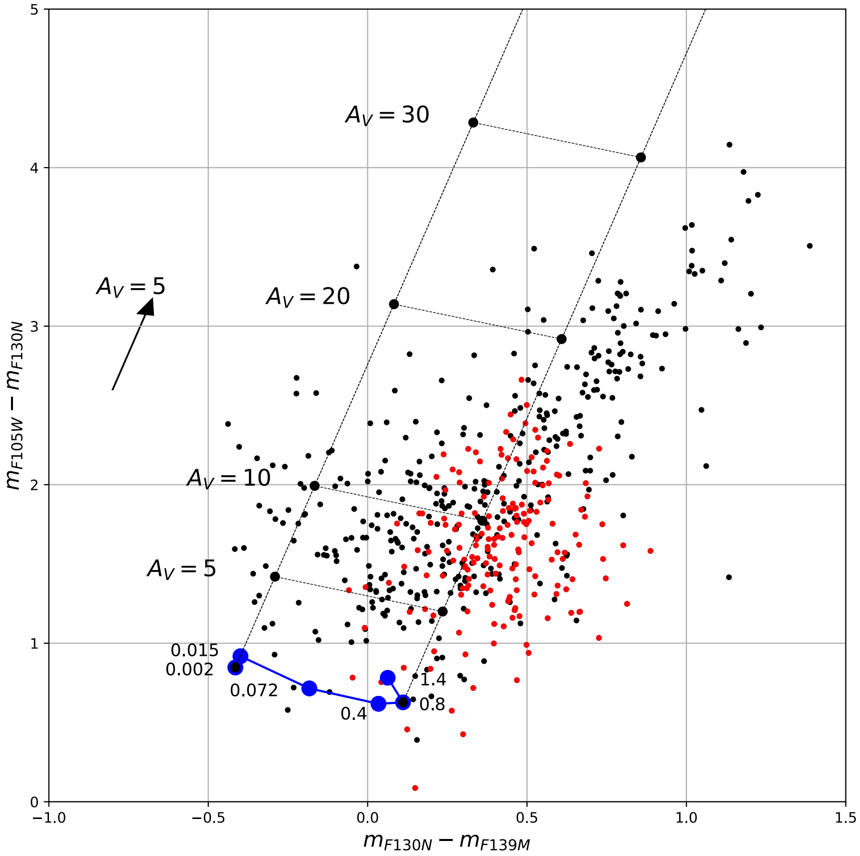

Figure 8. Color–color diagram for the sample of sources with magnitude error smaller than 0.2 in all three filters. The blue solid line represents the locus of the 1 Myr BT-Settl isochrone, with large blue dots drawn in correspondence with the masses reported in units of the solar mass. The black dotted straight lines are oriented along a standard $R_V = 3.1$ reddening vector (Cardelli et al. 1989), with reddening corresponding to $A_V = 5$, 10, 20, and 30 mag. The red dots indicate our candidate background sources.

in effective wavelength within the passbands. The effect is more pronounced in broadband filters and causes significant nonlinearity if the color is obtained by combining narrow and broad passbands, as the effective wavelengths remain nearly constant in the former and move significantly in the latter. Moreover, there is a tendency to reach saturation, i.e., as the extinction increases, the incremental variations of effective wavelengths become smaller and smaller. Also, the estimated change in source magnitude in each filter depends on the original spectral energy distribution of the source itself.

To assess the relevance of these factors, we have performed synthetic photometry in our photometric passbands probing different assumptions. Specifically, we have determined the change in our colors at $A_V = 5$, 10, 20, 30, 40, 50, and 60, for effective temperatures $T_{\rm eff} = 10{,}000$ K (a reference value for the Vega magnitude scale) and $T_{\rm eff} = 3000$ K (more representative of low-mass young stars) and for different reddening laws. The results are always a set of nonlinear relations like those presented in Figure 9, which generally better match the locus of the sources. The curves shown in Figure 9, plotted twice for the low-mass and high-mass ends of our 1 Myr isochrone, relate to four cases. There is a degeneracy, as one can readily discern: only two curves start from the same points: the leftmost relates to two cases with $T_{\rm eff} = 10{,}000$ K while the rightmost is for two cases at $T_{\rm eff} = 3000$ K. Their difference illustrates how the change in colors depends on the effective temperature of the stars, colder stars producing stronger deviations from the original slope, i.e., the tangent at $A_V = 0$.

The two cases calculated for $T_{\rm eff} = 10{,}000$ K probe two different R_V values for the same Cardelli et al. (1989) law: $R_V = 3.1$ (green squares) and $R_V = 2.5$ (black circles). We consider this second value following Damineli et al. (2016), who found that intracluster dust grains have properties different from the less dense interstellar medium, resulting in a reddening law steeper than the canonical one. They report a value $R_V = 2.5$ for the young stellar cluster Westerlund 1, one of the most massive young clusters in the Milky Way. While the two curves overlap, the lower R_V value produces higher A_V for the same color excess: black circles are always below the green squares. The larger estimated extinction resulting from the adoption of a lower R_V will lead to an increase in the estimated source luminosity and photospheric radius, and a younger isochronal age.

The other curve, for a 3000 K photosphere, is also the overlap of two different cases, i.e., two different families of reddening laws for the same $R_V = 2.5$ value: those of Cardelli et al. (1989, red squares) and Fitzpatrick (1999, black circles). The differences in this case are smaller, with the Fitzpatrick (1999) law predicting slightly higher A_V values for the same amount of reddening.

The extinction at near-IR wavelengths, $0.8\,\mu{\rm m} < \lambda < 2.4\,\mu{\rm m}$, is generally parameterized by a power law $A_\lambda \propto \lambda^{-\alpha}$ (Fitzpatrick 1999). As reported by Damineli et al. (2016), the

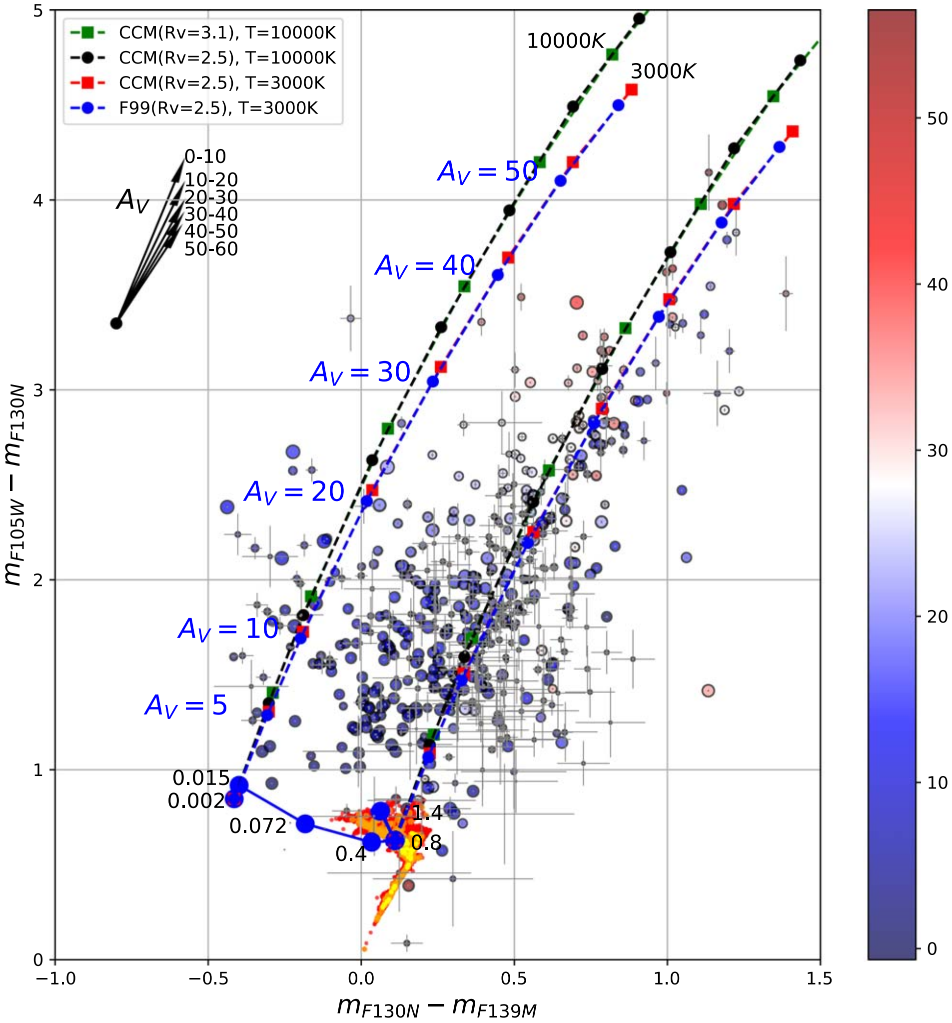

Figure 9. Color–color diagram for the sample of sources with magnitude error smaller than 0.2 in all three filters. The blue solid line represents the locus of the 1 Myr BT-Settl isochrone, with the correction for the F139M filter adopted by Robberto et al. (2020) and filled circles drawn in correspondence with the masses reported in units of the solar mass. The dashed lines represent the reddening curves determined through synthetic photometry, according to the parameters reported in the labels (see also text). On each curve the dots represent, from the isochrone up, the reddening corresponding to $A_V = 5$, 10, 20, 30, 40, 50, and 60 mag. The arrows represent the change in reddening vector for increasing ranges of extinction. The size of the circles is proportional to the magnitude in the F130N filter, whereas the colors are representative of the extinction according to the Fitzpatrick (1999) $R_V = 2.5$ reddening law, with the color scheme shown in the scale bar to the right. All error bars are plotted, and are derived from the uncertainties presented in Figure 3, but only those larger than the circle size are visible. The clump of colored dots (red, orange, and yellow colors tracing increasing source density) at the bottom of the figure represents the tip of the Galactic population derived from the Besançon models (Robin et al. 2003) for the celestial coordinates and extent of our NGC 2024 field. See Section 3.2 for details.

power-law exponent α can take a broad range of values, from 1.66 for the Cardelli et al. (1989) $R = 3.1$ reddening curve to $\alpha = 2.13$ for Westerlund 1, up to $\alpha = 2.64$ (González-Fernández et al. 2014). In our case the spectral coverage is admittedly narrow, but it is still interesting to check how α changes in our four reference cases, performing a best fit to our three extinction values. In order to maintain the same parameterization adopted by Damineli et al. (2016), we add to our synthetic estimates the K_s filter adopting the 2MASS passband. It is found that, for extinction values ranging from $A_V = 1$ to $A_V = 60$, α takes the following values:

1. $\alpha = 1.62$–1.78 for Cardelli et al. (1989) with $R_V = 3.1$ and $T_{\rm eff} = 10{,}000$ K
2. $\alpha = 1.62$–1.73 for Cardelli et al. (1989) with $R_V = 2.5$ and $T_{\rm eff} = 10{,}000$ K
3. $\alpha = 1.62$–1.77 for Cardelli et al. (1989) with $R_V = 2.5$ and $T_{\rm eff} = 3000$ K
4. $\alpha = 1.50$–1.61 for Fitzpatrick (1999) with $R_V = 2.5$ and $T_{\rm eff} = 3000$ K.

Overall the change is of the order of 10%. While the α value always increases with the extinction, the change is not enough, for our passbands, to move it to values as high as, e.g., $\alpha = 2.13$ with $A_V \sim 10$ as estimated by Damineli et al. (2016) for Westerlund 1 on the basis of broadband multicolor photometry.

In summary, as reddening increases, extinction increases nonlinearly. It takes a larger amount of extinction to produce the same increment in reddening or, in other words, the $R_\lambda = A_\lambda/(A_{\lambda_x} - A_\lambda)$ ratio decreases with A_λ. The correlation between R_λ and A_V is illustrated by the set of arrows in Figure 9, representing how the reddening vector changes in our color–color diagram, in both direction and modulus, when one increases A_V in steps of 10 mag. We shall consider hereafter two reference cases: the standard Cardelli et al. (1989) $R_V = 3.1$

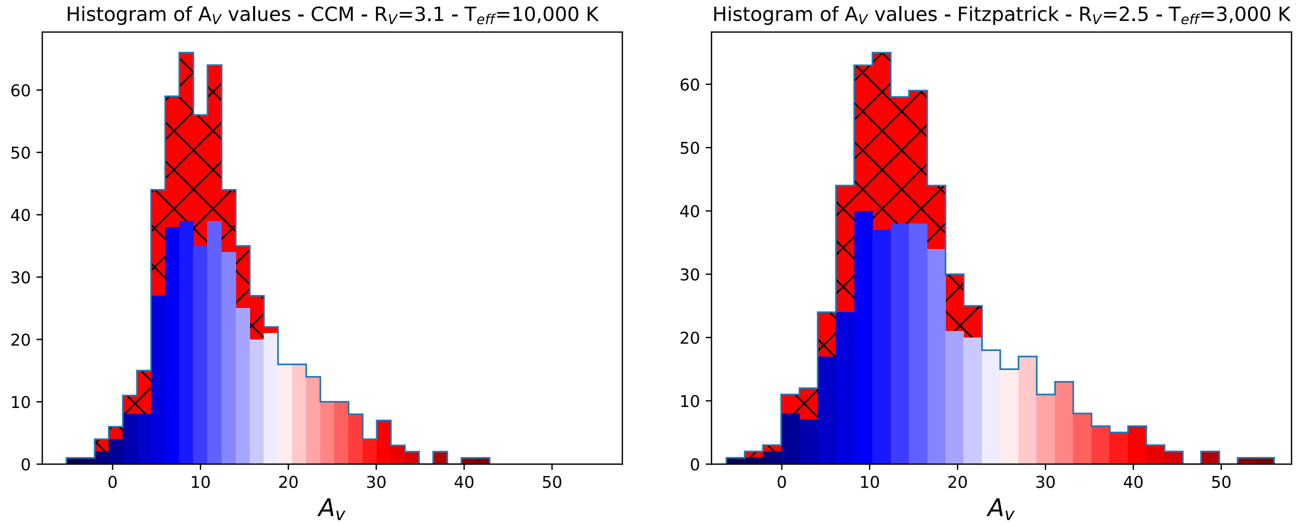

Figure 10. Histogram of the distribution of estimated A_V values according to the Cardelli et al. (1989, left) and Fitzpatrick (1999, right) reddening curves. For the cluster candidates the A_V values are color-coded using, for the Fitzpatrick case, the scale bar presented in Figure 9, while a similar one properly rescaled is used for the Cardelli et al. case . The cross-hatched area shows the background candidate sources, plotted on top of the cluster candidates.

law for $T_{\rm eff} = 10{,}000$ K and the Fitzpatrick (1999) $R_V = 2.5$ law for $T_{\rm eff} = 3000$ K, anticipating that the two assumptions will result in different parameters for the cluster population.

Adopting these laws, we obtain two estimates of the extinction toward each source using the following strategy. Tracing back the reddening curve, we deredden to the 1 Myr isochrone all cluster candidates lying in the central region between the two reddening curves drawn in Figure 9. Cluster candidates to the left and right of the central band require an approximate treatment, since there is no reddening curve, among those that we have considered and that correspond to a rather broad range of models, that can consistently explain their location on the diagram. We thus consider only their F105 – F130 color, as it combines two bandpasses centered on the photospheric continuum and, by producing the largest differences, is the one least affected by photometric uncertainties. To account for the intrinsic stellar color, we subtract from the measured F105 – F130 indices the color of a 0.8 $M_\odot$ star on our isochrone, which is almost coincident with the color of a 0.4 $M_\odot$ star. We verified that for the sources within the central region this approach produces A_V values close to those obtained with the full projection back to the isochrone. The same strategy is adopted for sources to the left of the central band, subtracting this time the color of a 0.015 $M_\odot$ dwarf.

The clump of colored dots at the bottom of Figure 9 represents the tip of the Galactic population derived from the Besançon models (Robin et al. 2003) for the celestial coordinates and extent of our NGC 2024 field. Running the Besançon simulator, we have maintained the default parameters and removed cuts on distance and apparent magnitudes that may bias the results, resulting in the full sample of about 22,500 stars. The photometry in our bandpasses was derived assuming for each model star the Phoenix spectrum (Husser et al. 2013) appropriate for the given effective temperature and surface gravity and accounting for the stellar luminosity and distance from the Sun. Considering that the locus of a 0.8 $M_\odot$ star is nearly coincident with the peak of the Besançon distribution (the tip of the yellow area in Figure 9), we deproject to this point all background candidate sources, regardless of their position in the diagram. For those lying within the central band, the difference between the extinction values determined using this treatment and using a full deprojection to the isochrone is generally small.

In producing Figure 9 we have color-coded each source according to the extinction values derived as we just described using the Fitzpatrick (1999) law. A color code based on the Cardelli et al. (1989) law would produce almost exactly the same diagram, with the exception of the scale bar with maximum at $A_V = 42$.

In Figure 10 we present the histograms of the A_V distribution. The candidate cluster members have been color-coded using scales analog to the one adopted for Figure 9, whereas the candidate background sources have been plotted using a red cross hatched pattern on top of the cluster distribution. The two plots are similar, with the Fitzpatrick (1999) law producing higher A_V values. In each plot the maximum is about the same for both the cluster and background populations. There are no highly reddened background sources, which is arguably a selection effect as we are not considering the faintest sources with large photometric error (i.e., the gray dots at the bottom of the diagrams in Figure 6), which in the CMDs generally fall in the clump of contaminants.

Figure 11 shows the spatial distribution of the sources, color-coded according to the Fitzpatrick (1999) law. Again, a nearly identical plot can be obtained using the Cardelli et al. (1989) law, with the exception of the compressed scale bar. The map confirms that the most highly reddened sources are concentrated at the center, while the sources with modest reddening are concentrated to the west, consistent with previous findings that the region to the west of the dark filament is less obscured and possibly more evolved. The candidate background sources are scattered around, with some clustering at the southern and western corners of the field, suggesting that these are regions where the underlying molecular cloud has lower optical depth.

3.3. Luminosity Function

Using the estimated extinction values, one can produce dereddened versions of the original CMDs presented in Figure 6. In particular, in Figure 12 we show the dereddened F130N versus F130N – F139M CMDs, for our two reference

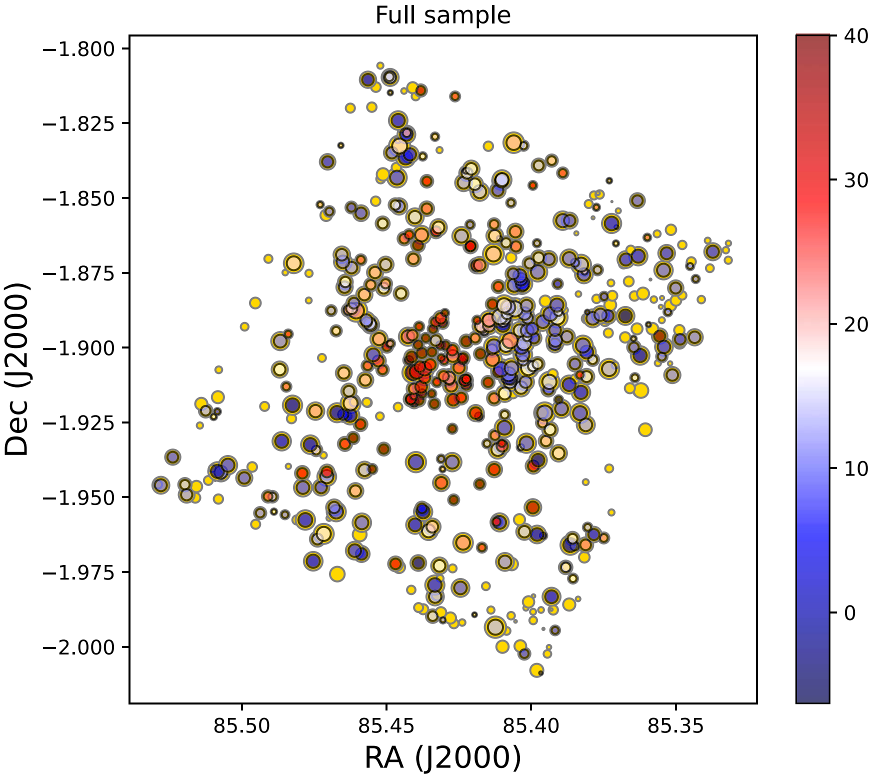

Figure 11. Map of the detected sources color-coded according to A_V. The scale bar is relative to the Fitzpatrick (1999) law.

extinction laws. Each diagram shows again the BT-Settl 1 Myr isochrone (blue dashed line) with the four large dots indicating the locus of 0.4, 0.072, 0.015, and 0.002 $M_\odot$ objects. We distinguish between the NGC 2024 cluster candidate population (black dots), dominating the upper part of the diagram, and the sources classified as candidate background stars (blue dots), concentrated in the lower part of the diagram. In both diagrams the two groups appear well separated, with few interlopers at the fringes of their distributions. Using the Fitzpatrick (1999) law, the dereddened magnitudes of all sources are found to be brighter by a couple of magnitudes than those derived using the Cardelli et al. (1989) law. The F130N – F139M colors instead are similarly distributed, and for the cluster candidates they become increasingly negative going to fainter magnitudes. Also, this diagram thus confirms the presence of H_2O in absorption in low-mass objects.

As in Figure 9, we use colored dots to represent the Galactic population estimated from the Besançon model of the Milky Way. Plotting these points, we added to the synthetic photometry of each star an error randomly extracted from the histograms presented in Figure 5, considering only sources in a ±0.1 wide bin centered around the source's magnitude. The model predicts for the few, brightest Besançon sources $m_{\mathrm{F130N}} \simeq 14$, whereas our candidate sources are about 1 mag brighter and fainter for the Fitzpatrick (1999) and Cardelli et al. (1989) laws, respectively. Colors are more spread than those of the Besançon population. One has to consider that photometric uncertainties directly affect not only the measured colors—an effect we have accounted for by spreading the Besançon data—but also the estimated extinction derived from Figure 9, which is sensitive to colors. This is a source of uncertainty we did not account for. Note also that the blue dots appear more scattered on the right side of the Besançon distribution for both extinction laws. Having a fraction of sources with some residual redder color may suggest that when we assumed for all of them the intrinsic colors of a star at the tip, rather than the tail, of the yellow area in Figure 9, we may have occasionally underestimated extinction.

The histograms of the dereddened F130N magnitudes are shown in Figure 13. Plotting the values for the cluster candidates, we distinguish between the full set of 397 sources (light blue) and an extinction-limited sample (dark blue) containing the 50% of sources with lower extinction. We also plot the background contaminants (red hatched area). The bins are equally spaced in magnitude by an amount corresponding to a change in brightness by a factor of 2. The scale at the top of the plot also shows the mass values according to the 1 Myr BT-Settl isochrone at 400 pc distance, which is obviously applicable only to the NGC 2024 sample.

As explained in Section 2, we cannot perform a reliable completeness correction at the faint end. We can focus instead on the brighter stars, i.e., the left side of the histograms free from background contamination. Referring for convenience to the mass scale, the IMF resulting from the Fitzpatrick (1999) law appears heavily loaded toward high masses compared with a conventional distribution such as, e.g., the realization of the Kroupa IMF (Kroupa et al. 2001), also shown in both figures as a dashed line. The extinction-limited sample also presents the same peak shifted to masses higher than the Kroupa IMF, but with a steeper slope than the full sample. The Cardelli et al. (1989) law (right plot) produces instead an IMF in better agreement with the Kroupa IMF, for both the full sample and especially the extinction-limited sample. Comparing the two diagrams, we can conclude that the Fitzpatrick (1999) law with $R_V = 2.5$ for $T_{\mathrm{eff}} = 3000$ K does not seem applicable to the case of NGC 2024. In Table 3 we present the extinction and mass

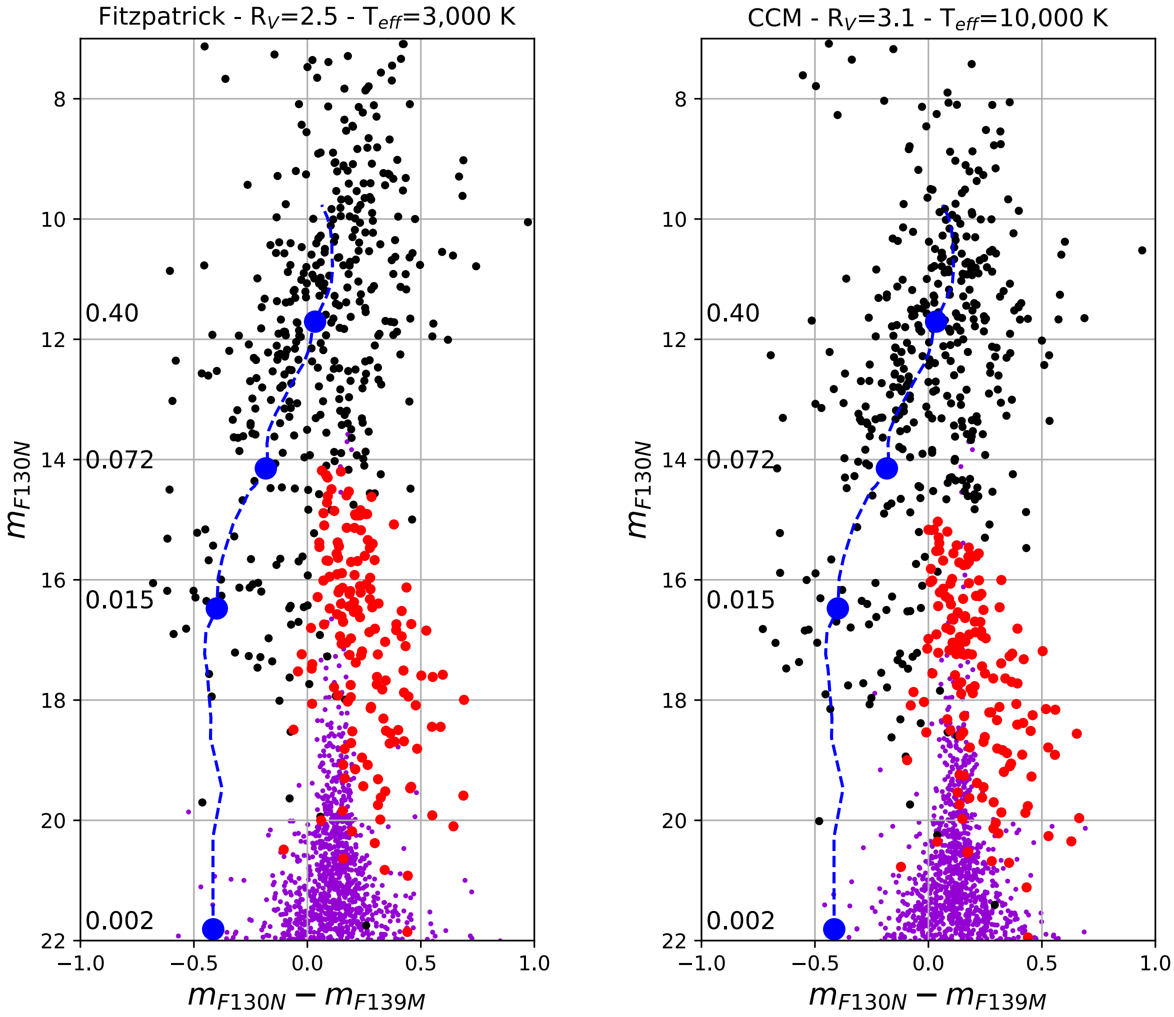

Figure 12. CMDs of the dereddened sources with magnitude error smaller than 0.2 in all three filters, after applying the reddening laws of Fitzpatrick (1999) with $R_V = 2.5$ (left) and Cardelli et al. (1989) with $R_V = 3.5$ (right). The blue dashed line represents the locus of the 1 Myr BT-Settl isochrone, with the correction for the F139M filter adopted by Robberto et al. (2020). Filled circles mark the masses reported on the left axis, in units of the solar mass. The red circles indicate the background candidate sources, while the purple dots mark the full sample of sources simulated by the Besançon model converted to our filters using the Phoenix models.

Table 3
Extinction and Mass of Candidate Cluster Members

Entry Nr.	A_V	$M/M_\odot$
1	4.75	0.04
3	6.70	0.014
8	6.89	0.008
…	…	…

Note. Values estimated adopting the Cardelli et al. (1989) $R_V = 3.1$ reddening law.

(This table is available in its entirety in machine-readable form.)

values estimated for the candidate cluster members using the Cardelli et al. (1989) law.

Still, also with the Cardelli et al. (1989) law there is an apparent excess of high-luminosity sources. A Wilcoxon rank-sum test shows a ≃10% probability that the full sample can be randomly extracted from a Kroupa IMF. The fact that the excess is more evident for the full sample points to a correlation between extinction and luminosity. The presence of such a correlation can be expected, since any overestimate of the extinction naturally leads to an overestimate of the intrinsic stellar luminosity, and vice versa. In this case the effect must be systematic, and looking at the two CMDs in Figure 6 one may discern a higher density of dots along a line parallel to and above the 1 Myr isochrone. This clumping is clearer in the Fitzpatrick (1999) diagram between $m_{130} = 10$ and 13, about two magnitudes above the isochrone, but it may still be visible on the right diagram, with larger scatter. This could indicate that the 1 Myr isochrone, the youngest available for the BT-Settl class of models, may not be ideal for a very young, deeply embedded cluster. The older D'Antona & Mazzitelli (1994) models pushed the calculations to earlier times, showing that the luminosity of a $0.4\,M_\odot$ star decreases by about 50% as it evolves from 0.5 to 1 Myr.

Of course, when positing younger ages for the stars in NGC 2024, one should take into account that mass accretion rates should also be higher, contributing to both the stellar luminosity and the actual pre-main-sequence evolution (see, e.g., Tout et al. 1999, for a discussion). Future JWST observations aimed at the determining the spectral type, surface gravity, and reddening of each source will shed light on the

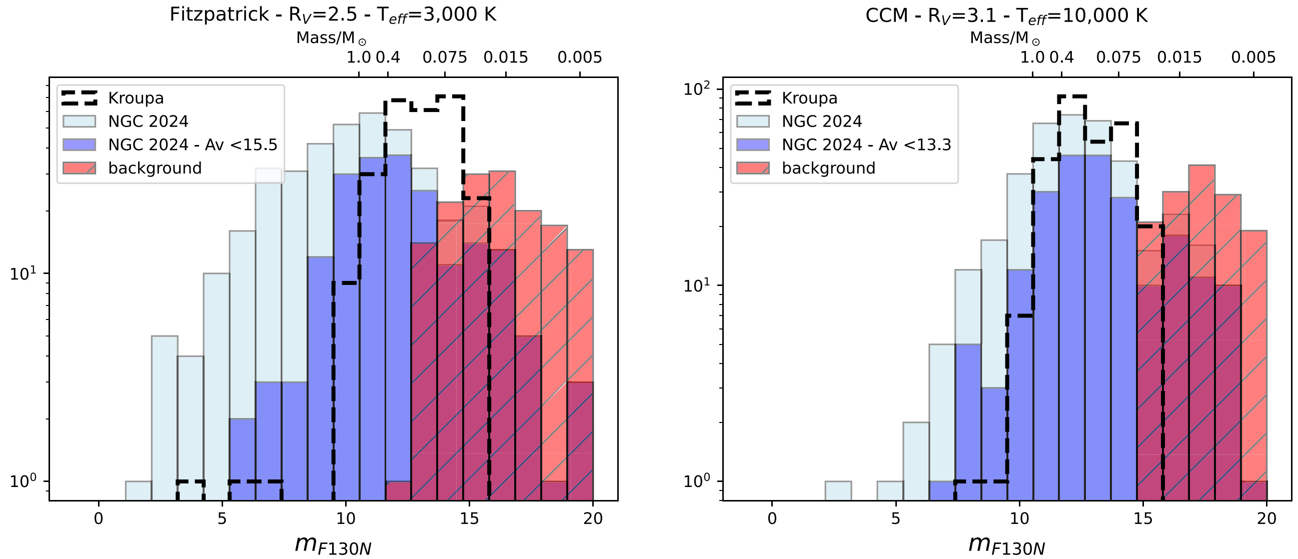

Figure 13. F130N luminosity functions for the candidate cluster members, both the full sample (light blue) and the extinction-limited sample (dark blue), together with the background sources (red hatched area). The top axis shows the masses corresponding to the F130N magnitudes according to the 1 Myr BT-Settl model, for an assumed distance of 400 pc. A random realization of the Kroupa IMF (Kroupa et al. 2001) for the number of stars in the extinction-limited sample is also plotted as a dashed line. The left plot is relative to the masses estimated using our baseline reddening law (Fitzpatrick 1999, with $R_V = 2.5$ and $T_{\rm eff} = 3000$ K), whereas the plot to the right is relative to the reddening curve derived from Cardelli et al. (1989) with $R_V = 2.5$ and $T_{\rm eff} = 10{,}000$ K.

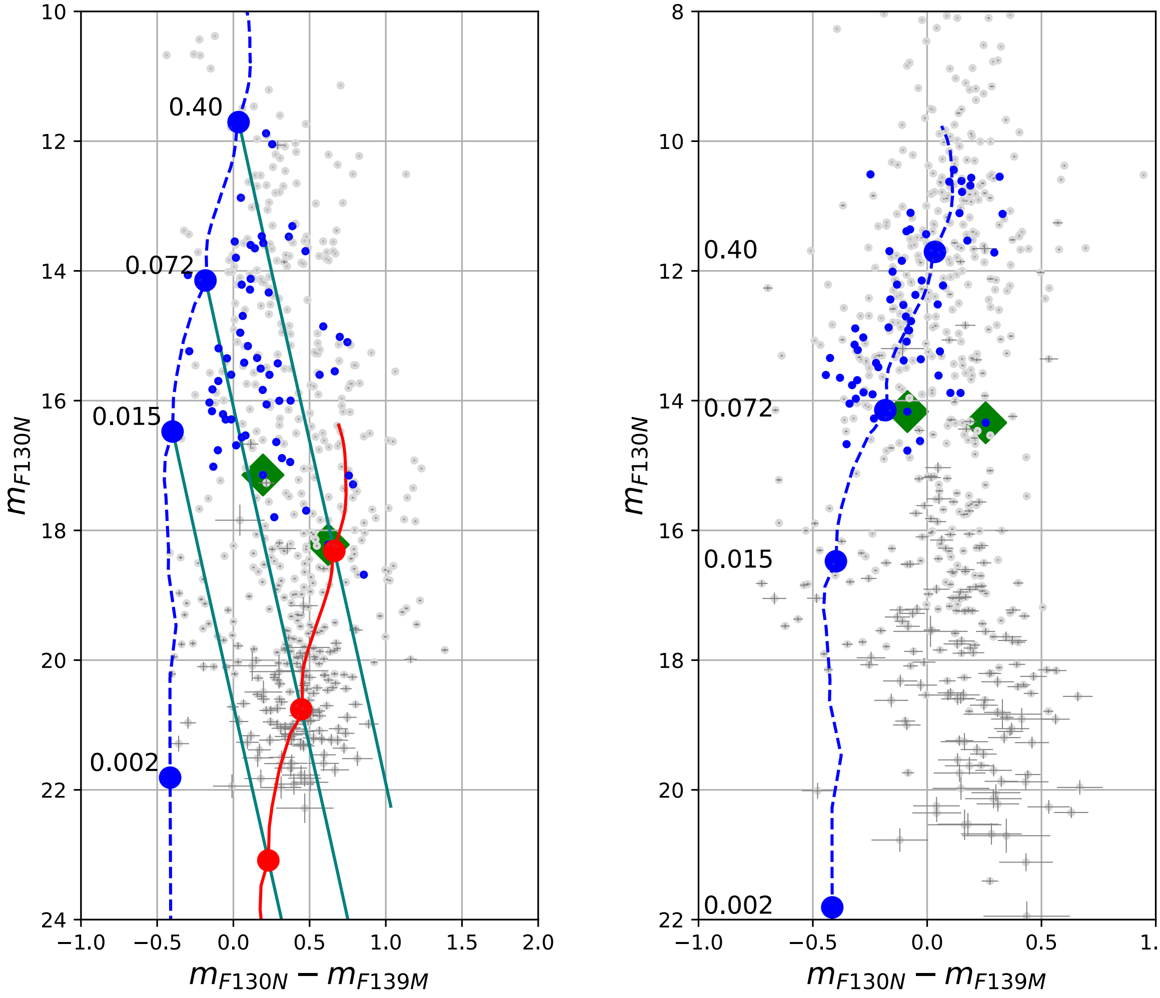

Figure 14. Left: the F130N vs. F130N – F139M CMD presented in Figure 6 (left), relating to the sources before reddening correction, is shown here for the full sample (gray dots). Blue dots indicate the sources targeted by the spectroscopic survey of Levine et al. (2006). Green diamonds represent the two sources classified by Levine et al. (2006) as background M giants. The green solid lines trace the extinction curves according to the Cardelli et al. (1989) reddening law, drawn from the positions of 0.4, 0.072, and 0.015 $M_\odot$ objects on the 1 Myr isochrone without extinction (blue dashed line) to the same isochrone with $A_V = 15$. Right: the same diagram after reddening correction (see also the right diagram in Figure 12), with blue dots indicating the sources targeted by the spectroscopic survey of Levine et al. (2006). The green diamonds again represent the two sources classified by Levine et al. (2006) as background M giants.

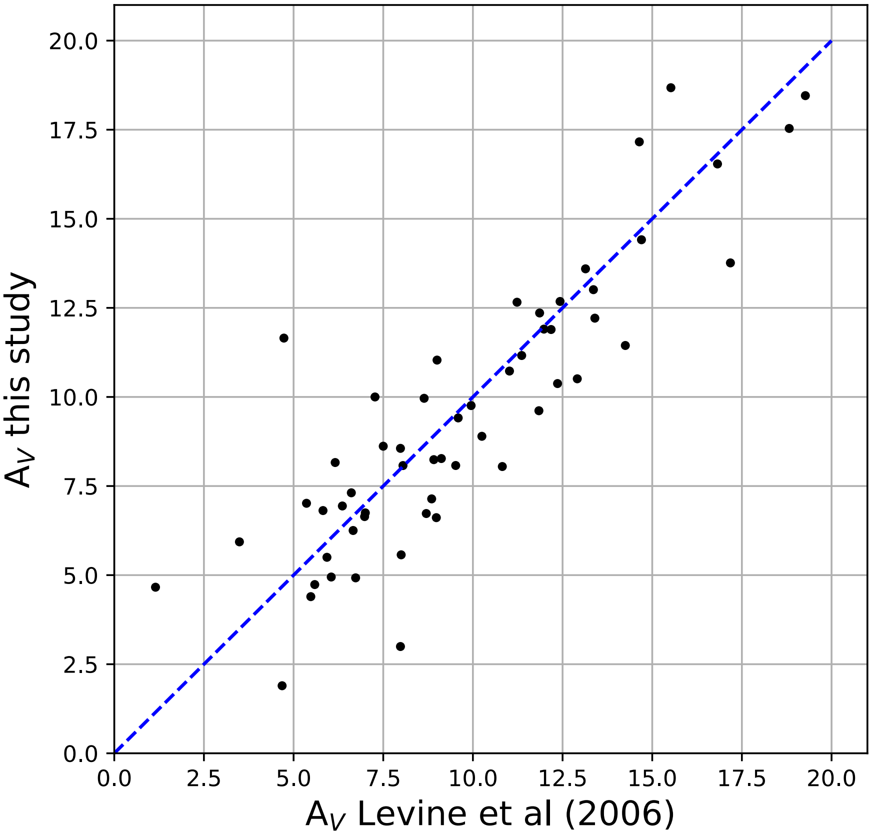

Figure 15. Comparison between the A_V values obtained using the WFC3 photometry in the F139M filter with our baseline reddening law and the values derived by Levine et al. (2006) using ground-based near-IR spectroscopy.

cause of the apparent excess of high-luminosity stars in NGC 2024 and in general on the IMF of this extremely young and deeply embedded cluster.

4. Comparison with IR Spectroscopy from Levine et al. (2006)

In their near-infrared photometric and spectroscopic study of NGC 2024 Levine et al. (2006) classified about 70 sources using the *J*- and *H*-band water absorption features, deriving spectral types in the range ~M1 to later than M8. Performing ground-based spectroscopy, the classification of infrared spectra based on the actual depth and width of the 1.4 μm H_2O feature is possible only for the brightest sources, as telluric absorption allows one to measure only the slope and depth of the short-wavelength fall-off at 1.35 μm. Still, combining this information with that coming from the shape of the 1.68 μm feature in the *H* band, Levine et al. (2006) managed to classify their sample with typical errors of 0.5–1 subtypes. This provides us with an independent test of our photometric classification method.

Figure 14 (left) shows the same data as presented in Figure 6 (left), i.e., the observed magnitude and color, with the sources classified by Levine et al. (2006) indicated as red dots. They occupy the upper part of the diagram, as expected due to the significant difference in sensitivity between ground-based spectroscopy and HST imaging. Analyzing their sample, Levine et al. (2006) identified two sources (#60 and #64) that may be background M giants, represented in Figure 14 as green diamonds. Figure 14 (right) shows the data corrected for reddening, as in Figure 12. The Levine sources, shown here as blue dots, are clustered around the isochrone with dereddened magnitudes brighter than $m_{130} \simeq 14$, corresponding to the H-burning limit on our 1 Myr isochrone. The two candidate M giants lie at the tip of the region containing Galactic contaminants, consistent with the Levine et al. (2006) classification.

Comparing the stellar parameters estimated by Levine et al. (2006) with those we determined in the previous sections, one has to take into account the different assumptions regarding reddening law, intrinsic stellar colors, and families of evolutionary models. In Figure 15 we show the extinction values we derived using our Cardelli et al. (1989) reddening law versus those of Levine et al. (2006). They determined A_V by comparing their $J - H$ colors with those empirically determined by Leggett (1992), Leggett et al. (1996), and Dahn et al. (2002) and adopting the reddening law of Cohen et al. (1981), all to be consistent with their Flamingos photometric system. The plot shows strong correlation, no systematic differences, and an average scatter $A_V \simeq 2$ mag versus a mean value $A_V \simeq 10$ mag.

A more direct comparison is the one between the spectral types derived by Levine et al. (2006) and our H_2O spectral index, presented in Figure 16. Here our index has been dereddened using again the Cardelli et al. (1989) reddening curve. The plot shows some significant scatter, especially for positive values of our index, with the sources spectroscopically classified as early M-type (<M3) having index values ranging between −0.1 and 0.5. However, moving down and to the left in the plot, i.e., to lower mass and later spectral types where the absorption feature is more prominent, the correlation between spectral type and spectral index becomes stronger, with a standard deviation of about one

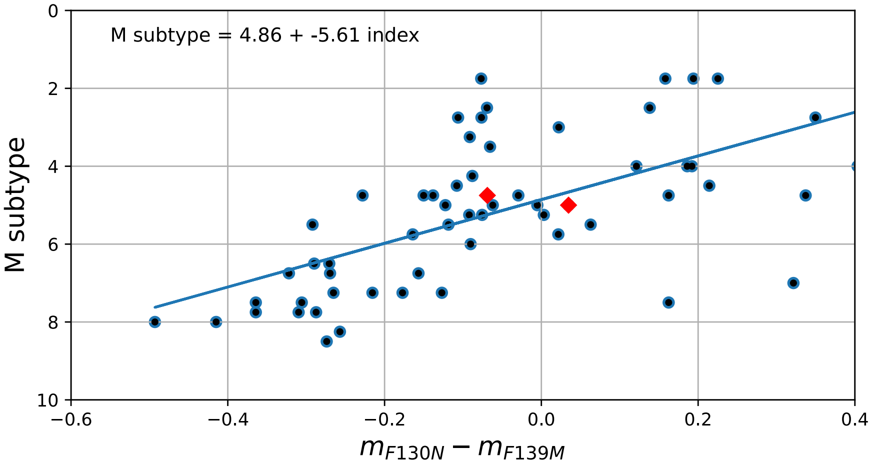

Figure 16. Spectral classification reported by Levine et al. (2006) vs. the color index determined using our WFC3 photometry.

subtype. The linear fit plotted in Figure 16, with parameters shown on the plot, has been determined using all available data.

5. Conclusion

We have presented the results of a survey of the young ($\lesssim$1 Myr) stellar cluster NGC 2024 associated with the Flame Nebula in Orion. The data, taken with the Wide Field Camera 3 on HST, probe the 1.4 μm H_2O absorption feature to discriminate the population of substellar objects, down to a few $M_{\rm Jup}$, against highly reddened, more massive stars.

In a field of about 85 arcmin^2 we detect 808 point sources, 550 of them having S/N>5 in all three filters. We estimate the reddening of this smaller sample using a distance-independent two-color diagram, finding that the source distribution cannot be explained by trivially adopting a linear relation between color and extinction based on any of the standard reddening laws. Instead, given the high extinction, one has to account for the change in effective wavelength as the extinction increases. We therefore used synthetic photometry to show that the nonlinearity of the reddening correction generally matches the distribution of the sources in the diagram and results in higher A_V values as the reddening increases. Adopting two different reddening laws, the Fitzpatrick (1999) law with $R_V = 2.5$ for a stellar photosphere at $T_{\rm eff} = 3000$ K and the Cardelli et al. (1989) law with $R_V = 3.1$ for a stellar photosphere at $T_{\rm eff} = 10{,}000$ K, we compare the resulting distributions of extinction values, which generally peak at $A_V \sim 15$ mag. The majority of highly reddened sources appear concentrated in the central part of the field, which is dominated at visible wavelengths by an extended dark lane. We then reconstruct the dereddened color–magnitude diagrams and derive the luminosity histograms, plotting both the full sample of candidate cluster members and the extinction-limited subsample containing 50% of the sources. We find that the Fitzpatrick (1999) law, overestimating the extinction, produces an excess of luminous (therefore massive) stars not compatible with the standard Salpeter slope of the IMF. The Cardelli et al. (1989) law is in much better agreement with the canonical IMF slope, but still shows an excess of luminous stars in the full sample, which includes the highly reddened sources. The correlation between high extinction and luminosity may result from a residual underestimate of the extinction. On the other hand, we posit that the correlation may be real and due to the most embedded sources being younger and overluminous compared with the more evolved and less extincted cluster stars in the foreground. We compare our classification scheme based on the depth of the 1.4 μm photometric feature with the results from the spectroscopic survey of Levine et al. (2006), finding general agreement especially for the late M subtypes, where the H_2O absorption feature is more prominent. Finally, we report a few peculiar sources and morphological features typical of the rich phenomenology commonly encountered in young star-forming regions.

Acknowledgments

Based on observations with the NASA/ESA/CSA Hubble Space Telescope obtained Mikulski Archive for Space Telescopes (MAST) at the Space Telescope Science Institute, which is operated by the Association of Universities for Research in Astronomy, Incorporated, under NASA contract NAS5- 26555. Support for Program number HST-GO-15334 was provided through grant HST-GO-15334.002-Av from the STScI under NASA contract NAS5-26555. The specific observations analyzed can be accessed via doi:10.17909/2ya9-db87. This work has made use of data from the European Space Agency (ESA) mission Gaia (https://www.cosmos.esa.int/gaia), processed by the Gaia Data Processing and Analysis Consortium (DPAC, https://www.cosmos.esa.int/web/gaia/dpac/consortium). Funding for the DPAC has been provided by national institutions, in particular the institutions participating in the Gaia Multilateral Agreement. We wish to acknowledge the anonymous referee for the helpful comments that helped to improve the manuscript.

Appendix
Individual Sources and Peculiar Morphological Features

Our choice of filters, aimed at discerning low-mass objects through the presence of H_2O molecular absorption and estimating their reddening, is less than ideal to trace the rich phenomenology generally associated with star-forming regions, which is better unveiled through narrowband imaging in recombination lines. Still, visual inspection of the images reveals, especially in the western part of the nebula less affected by extinction, a number of features worthy of being reported.

Source IRS 1 appears encircled by an extended cavity about 3′ or 1/3 of a parsec long, with edges traced by narrow, dark

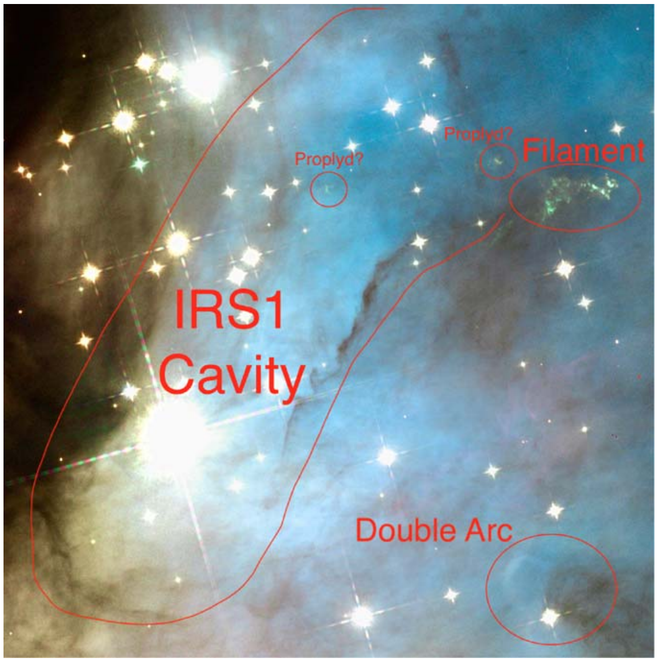

Figure 17. Enlargement of the cavity surrounding the IRS 1 region, with the positions of the proplyds, filaments, and arcs described in Figures 12, 13, and 14.

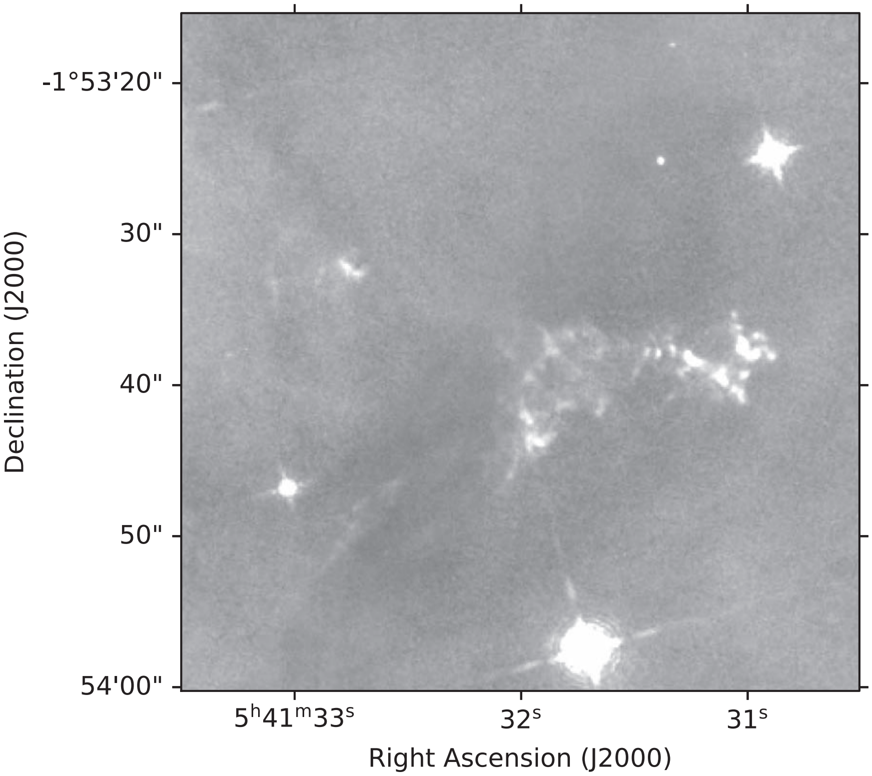

Figure 18. Zoom-in on the filamentary structure to the northwest of IRS 1, with the photoionized disk also visible in the upper left quadrant.

filaments (Figure 17). Proplyds 1 and 2 of Haworth et al. (2021) lie inside this cavity in the vicinity of IRS 1, consistent with their direct exposure to strong ultraviolet radiation; in our images they appear as point sources without any evidence of circumstellar material, proplyd 2 being coincidentally well aligned with a diffraction spike from IRS 1. The two other proplyds and the four candidate proplyds detected by Haworth et al. (2021) do not appear in our images.

At the northwestern end of the IRS 1 cavity, a complex filamentary structure (Figure 18) approximately centered at R.A. = 05:41:31.4, decl. = −01:53:38 (J2000.0) is most probably the working surface of a protostellar jet from an unidentified source. The filament is most prominent in the F130N filter. Nominally, this is a line-free filter, i.e., the Paschen-beta continuum, centered at 1300 nm with FWHM of 20 nm. The steep, blue cutoff of the filter at 1290 nm should prevent the

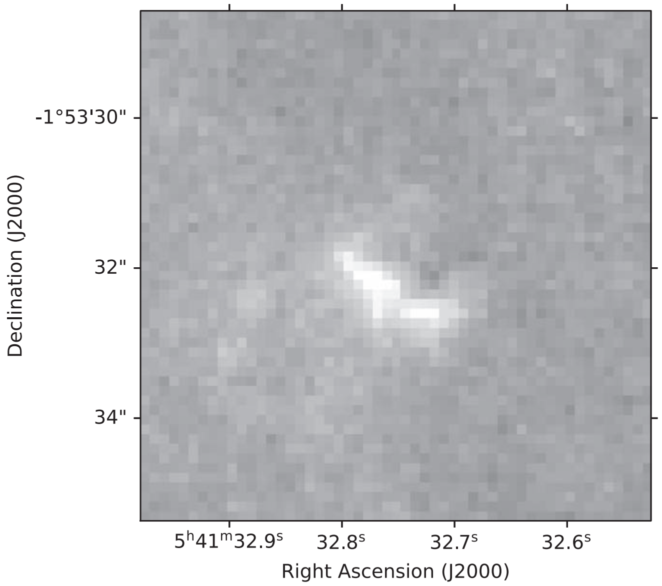

Figure 19. Zoom-in on the binary proplyd at R.A. = 05:41:32.7, decl. = –01:53:32. This image and the following ones are all in the F130N passband.

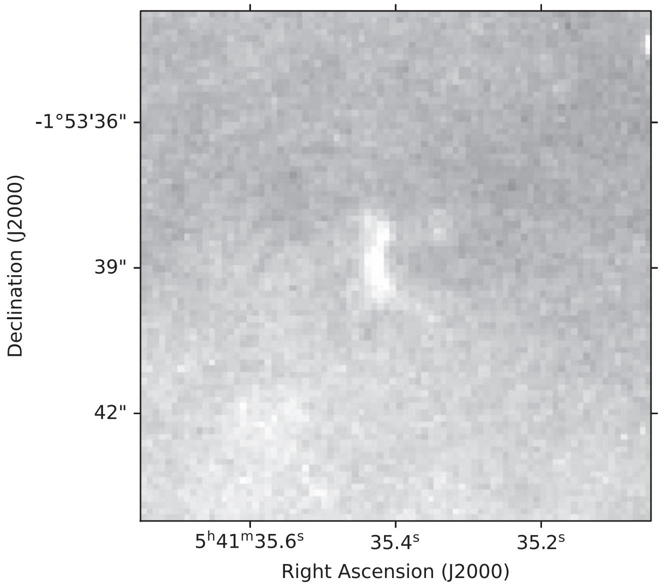

Figure 20. Zoom-in on the proplyd within the IRS 1 cavity at RA = 05:41:35.1, decl. = –01:53:39.

1282 nm Paschen-beta line from entering the passband, but our data suggest that some contamination may be present.

Two other sources in the area show proplyd-like morphology. In particular at R.A. = 05:41:32.75, decl. = –01:53:32.0 (J2000.0), about 10″ to the northeast of the jet and within the field shown in Figure 18, a compact extended source is characterized by a bright rim perpendicular to the direction of IRS 1. The enlargement shown in Figure 19 reveals that the rim may be broken into two parts, and one may recognize faint emission from the rear side opposite IRS 1, two compact jets protruding through the ionized rim, and possibly two darker areas where one could expect to find dark disks, a morphology that would be consistent with a binary proplyd. A second compact arc of emission (Figure 20) also consistent with the presence of a proplyd, is visible within the boundaries of the cavity at R.A. = 05:41:35.4, decl. = –01:53:39 (J2000.0).

To the southwest of the cavity, a striking feature is a double pillar with bright and dark components that appears aligned toward IRS 1 (Figure 21). A tempting explanation is that the bright arc traces the rim of a pillar illuminated by IRS 1, a pillar that casts its shadow onto a translucent veil behind it, which therefore traces in silhouette the morphology of the underlying illuminated structure, providing us with a rare direct glimpse of the 3D structure of the region.

At the northern edge of our survey field, our source #810 (2MASS J05413744-0149532) at R.A. = 05:41:37.4, decl. = −01:49:53.7 (J2000.0) is encircled by a $6'' \times 9''$ ellipsoidal cavity with sharp inner boundaries and no indication of bipolar morphology (Figure 22).

Also in the vicinity of the northern edge of our survey field, a source at R.A. = 05:41:38.44, decl. = -01:50:38.5 (J2000.0) is resolved into a peculiar triple system of nearly coaligned stars of almost equal brightness ($m_{130} \simeq 13.0$ mag) (Figure 23). These sources (#776, 778, and 780 in our catalog) have $\simeq 0\farcs8$ separation between each pair, corresponding to a projected distance of about 320 au.

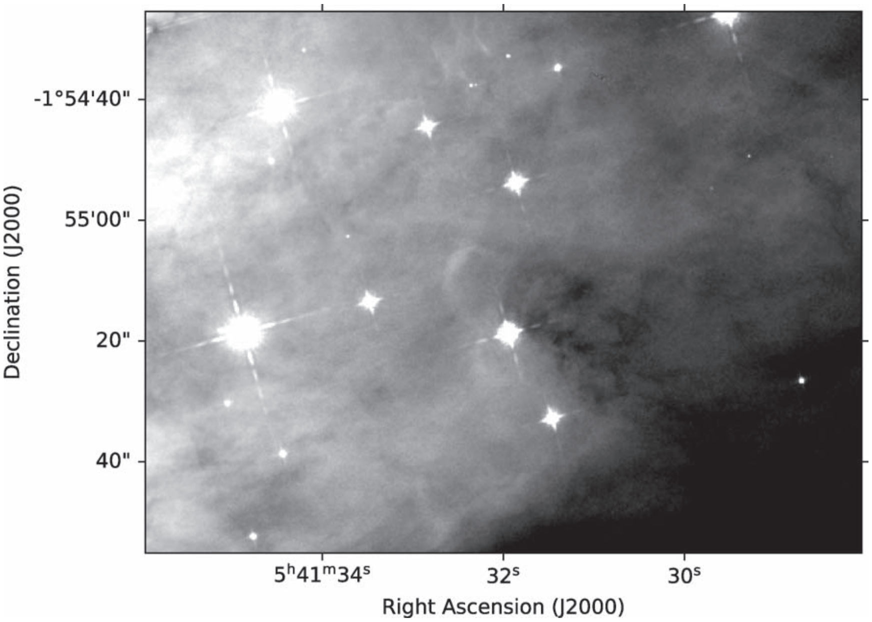

Figure 21. Zoom-in on the double arc to the west of IRS 1.

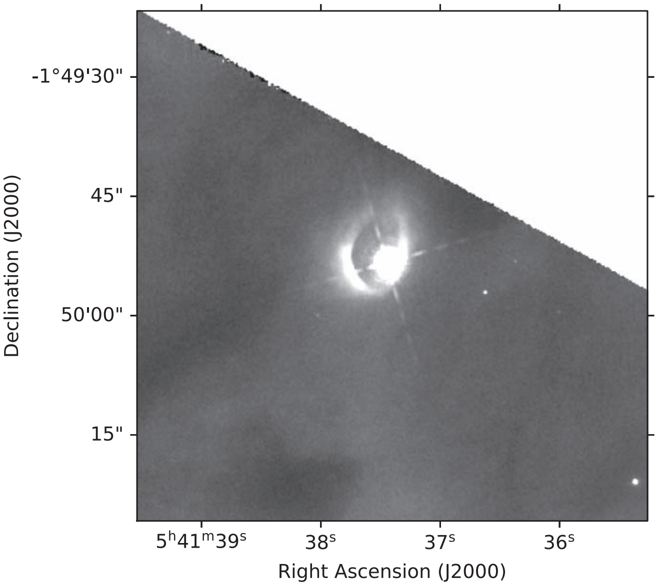

Figure 22. Zoom-in on 2MASS J05413744-0149532 with its surrounding cavity.

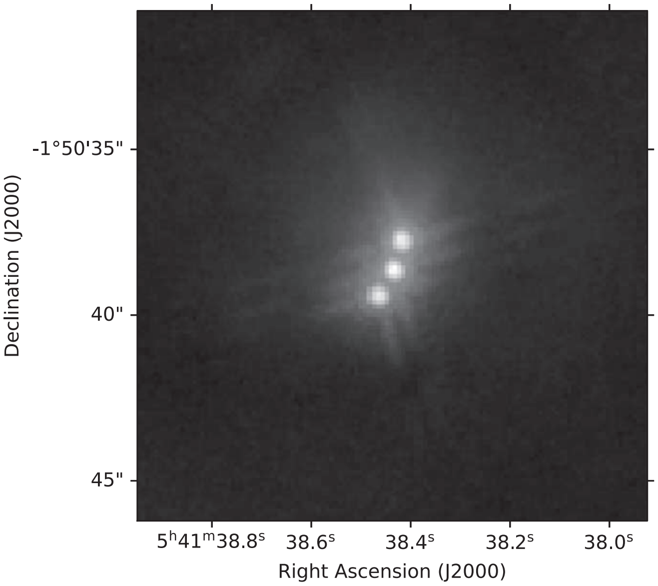

Figure 23. Zoom-in on a remarkable triple system.

ORCID iDs

Massimo Robberto https://orcid.org/0000-0002-9573-3199
Mario Gennaro https://orcid.org/0000-0002-5581-2896
Giovanni Maria Strampelli https://orcid.org/0000-0002-1652-420X
Elena Sabbi https://orcid.org/0000-0003-2954-7643
Dana Koeppe https://orcid.org/0000-0001-6903-3108
Jonathan C. Tan https://orcid.org/0000-0002-3389-9142
David R. Soderblom https://orcid.org/0000-0002-0322-8161

References

Almendros-Abad, V., Mužić, K., Bouy, H., et al. 2023, A&A, 677, A26
Bajaj, V., Calamida, A., & Mack, J. 2022, AJ, 164, 32
Barnes, P. J., Crutcher, R. M., Bieging, J. H., Storey, J. W. V., & Willner, S. P. 1989, ApJ, 342, 883
Bayo, A., Barrado, D., Stauffer, J., et al. 2011, A&A, 536, A63
Bik, A., Lenorzer, A., Kaper, L., et al. 2003, A&A, 404, 249
Bonnell, I. A., Clark, P., & Bate, M. R. 2008, MNRAS, 389, 1556
Brinkmann, N., Banerjee, S., Motwani, B., & Kroupa, P. 2017, A&A, 600, A49
Cardelli, J. A., Clayton, G. C., & Mathis, J. S. 1989, ApJ, 345, 245
Cohen, J. G., Frogel, J. A., Persson, S. E., & Elias, J. H. 1981, ApJ, 249, 481
Comeron, F., Rieke, G. H., & Rieke, M. J. 1996, ApJ, 473, 294
Cutri, R. M., Skrutskie, M. F., van Dyk, S., et al. 2003, VizieR Online Data Catalog: 2MASS All-Sky Catalog of Point Sources (Cutri+ 2003), VizieR Online Data Catalog
Dahn, C. C., Harris, H. C., Vrba, F. J., et al. 2002, AJ, 124, 1170
Damian, B., Jose, J., Biller, B., et al. 2023, ApJ, 951, 139
Damineli, A., Almeida, L. A., Blum, R. D., et al. 2016, MNRAS, 463, 2653
D'Antona, F., & Mazzitelli, I. 1994, ApJS, 90, 467
Dib, S. 2014, MNRAS, 444, 1957
Dib, S. 2022, A&A, 666, 113
Dib, S., Schmeja, S., & Hony, S. 2017, MNRAS, 464, 1738
Dib, S., Shadmehri, M., Padoan, P., et al. 2010, MNRAS, 405, 401
Dolphin, A., 2016, DOLPHOT: Stellar photometry, Astrophysics Source Code Library, ascl:1608.013
Dolphin, A. E. 2000, PASP, 112, 1383
Downes, J. J., Briceño, C., Mateu, C., et al. 2014, MNRAS, 444, 1793
Fitzpatrick, E. L. 1999, PASP, 111, 63
Gaia Collaboration, Brown, A. G. A., Vallenari, A., et al. 2016b, A&A, 595, A2
Gaia Collaboration, Prusti, T., de Bruijne, J. H. J., et al. 2016a, A&A, 595, A1
Gennaro, M., & Robberto, M. 2020, ApJ, 896, 80
González-Fernández, C., Asensio Ramos, A., Garzón, F., Cabrera-Lavers, A., & Hammersley, P. L. 2014, ApJ, 782, 86
Grudić, M. Y., Hopkins, P. F., Faucher-Giguère, C. A., et al. 2018, MNRAS, 475, 3511
Haisch, Karl E., & Lada, J. 2000, AJ, 120, 1396
Haworth, T. J., Kim, J. S., Winter, A. J., et al. 2021, MNRAS, 501, 3502
Hopkins, A. M. 2018, PASA, 35, 39
Husser, T. O., Wende-von Berg, S., Dreizler, S., et al. 2013, A&A, 553, A6
Kroupa, P. 2001, MNRAS, 322, 231
Kroupa, P., Aarseth, S., & Hurley, J. 2001, MNRAS, 321, 699
Krumholz, M. R., McKee, C. F., & Bland-Hawthorn, J. 2019, ARA&A, 57, 227
Lada, C. J., & Lada, E. A. 2003, ARA&A, 41, 57
Leggett, S. K. 1992, ApJS, 82, 351
Leggett, S. K., Allard, F., Berriman, G., Dahn, C. C., & Hauschildt, P. H. 1996, ApJS, 104, 117
Levine, J. L., Steinhauer, A., Elston, R. J., & Lada, E. A. 2006, ApJ, 646, 1215
Liu, W. M., Meyer, M. R., Cotera, A. S., & Young, E. T. 2003, AJ, 126, 1665
Lodieu, N. 2013, MNRAS, 431, 3222
Luhman, K. L. 2007, ApJ, 173, 104
Megeath, S. T., Flaherty, K. M., Hora, J., et al. 2005, in IAU Symp. 227, Massive Star Birth: A Crossroads of Astrophysics, ed. R. Cesaroni et al. (Cambridge: Cambridge Univ. Press), 383
Meyer, M. R. 1996, PhD thesis, Max-Planck-Institute for Astronomy, Heidelberg
Meyer, M. R., Flaherty, K., Levine, J. L., et al. 2008, in Handbook of Star Forming Regions, Volume I, ed. B. Reipurth (Bristol: IOP Science), 662
Mužić, K., Scholz, A., Geers, V. C., & Jayawardhana, R. 2015, ApJ, 810, 159
Offner, S. S. R., Clark, P. C., Hennebelle, P., et al. 2014, in Protostars and Planets VI, ed. H. Beuther et al. (Tucson: Univ. of Arizona Press), 53
Oliveira, C. A. D., Moraux, E., Bouvier, J., & Bouy, H. 2012, A&A, 539, A151
Peña, K., Ramírez, P. P., Béjar, V. J. S., et al. 2012, ApJ, 754, 30
Rivera-Ortiz, P. R., Rodríguez-González, A., Cantó, J., & Zapata, L. A. 2021, ApJ, 916, 56
Robberto, M., Gennaro, M., Ubeira Gabellini, M. G., et al. 2020, ApJ, 896, 79
Robin, A. C., Reylé, C., Derrière, S., & Picaud, S. 2003, A&A, 409, 523
Scholz, A., Geers, V., Clark, P., Jayawardhana, R., & Muzic, K. 2013, ApJ, 775, 138
Skinner, S., Gagné, M., & Belzer, E. 2003, ApJ, 598, 375
Stamatellos, D., & Whitworth, A. P. 2009, MNRAS, 392, 413
Störzer, H., & Hollenbach, D. 1999, ApJ, 515, 669
STScI Development Team, 2018 synphot: Synthetic photometry using Astropy, Astrophysics Source Code Library, ascl:1811.001
Suárez, G., Downes, J. J., Román-Zúñiga, C., et al. 2019, MNRAS, 486, 1718
Tout, C. A., Livio, M., & Bonnell, I. A. 1999, MNRAS, 310, 360
van Terwisga, S. E., van Dishoeck, E. F., Mann, R. K., et al. 2020, A&A, 640, A27
Weidner, C., Kroupa, P., & Pflamm-Altenburg, J. 2013, MNRAS, 434, 84
Whitworth, A., Bate, M. R., Nordlund, A, Reipurth, B., & Zinnecker, H, 2007, in Protostars and Planets V, ed. B. Reipurth, D. Jewitt, & K. Keil, Vol. 459 (Tucson: Univ. of Arizona Press), 459
Winter, A. J., Kruijssen, J. M. D., Chevance, M., Keller, B. W., & Longmore, S. N. 2020, MNRAS, 491, 903